Journal of Nuclear Medicine, published on April 9, 2021 as doi:10.2967/jnumed.121.262122

Dosimetric evaluation of receptor-heterogeneity on the therapeutic efficacy of peptide receptor radionuclide therapy: correlation with DNA damage induction and *in vivo* survival

Giulia Tamborino[1,2], Julie Nonnekens[2,3,4], Marijke De Saint-Hubert[1], Lara Struelens[1], Danny Feijtel[2,3], Marion de Jong[2] and Mark W. Konijnenberg[2†]

[1]*Research in Dosimetric Application, Belgian Nuclear Research Centre (SCK CEN), Mol, Belgium.*
[2]*Department of Radiology & Nuclear Medicine, Erasmus MC, Rotterdam, The Netherlands.*
[3]*Department of Molecular Genetics, Erasmus MC, Rotterdam, The Netherlands.*
[4]*Oncode Institute, Erasmus MC, Rotterdam, The Netherlands.*

[†]Corresponding author: **Mark W. Konijnenberg**, Department of Radiology & Nuclear Medicine, ERASMUS MC, Room Ns-561, PO box 2040, 3000 CA, Rotterdam, The Netherlands, Tel: +31(0)612280668, Email: m.konijnenberg@erasmusmc.nl

First author: **Giulia Tamborino**, Research in Dosimetric Application, Belgian Nuclear Research Centre (SCK CEN), Boeretang 200, 2400 Mol, Belgium, Tel: +32 471 99 66 09, Email: gtambori@sckcen.be, PhD student.

Words: 5505

Financial support: None

Running title: Dose-response for *in vivo* PRRT

ABSTRACT

Rationale: To build a refined dosimetry model for [^{177}Lu]Lu-DOTA-[Tyr^3]octreotate (^{177}Lu-DOTATATE) *in vivo* experiments enabling the correlation of absorbed dose with double strand breaks (DSBs) induction and cell death. **Methods:** Somatostatin receptor type-2 ($SSTR_2$) expression of NCI-H69 xenografted mice, injected with ^{177}Lu-DOTATATE, was imaged at 0, 2, 5, 11 days. This was used as input to reconstruct realistic 3 dimensional heterogeneous activity distributions and tissue geometries of both cancer and heathy cells. The resulting volumetric absorbed dose rate distributions were calculated using GATE Monte Carlo code and compared to homogenous dose rate distributions. The absorbed dose (0-2 days) on μm-scale sections was correlated with DSBs induction, measured by γH2AX foci. Moreover, the absorbed dose on larger mm-scale sections delivered over the whole treatment (0-14 days) was correlated to the modelled *in vivo* survival to determine the radiosensitivity parameters α and β for comparison with experimental data (cell death assay, volume response) and external beam radiotherapy (EBRT). The DNA-damage repair half-life T_μ and proliferation doubling time T_D were obtained by fitting the DSBs and tumor volume data over time. **Results:** A linear correlation with a slope of 0.0223 DSBs/cell mGy^{-1} between the absorbed dose and the number of DSBs/cell has been established. The heterogeneous dose distributions differ significantly from the homogenous dose distributions, with their corresponding average S-values diverging at 11 days up to +58%. No significant difference between modelled *in vivo* survival is observed in the first 5 days when using heterogeneous and uniform dose distributions, respectively. The radiosensitivity parameter analysis for the *in vivo* survival correlation indicates that the minimal effective dose rates for cell kill are 13.72 mGy/h and 7.40 mGy/h, with α=0.14 Gy^{-1} and 0.264 Gy^{-1}, respectively and α/β=100 Gy; decreasing the α/β leads to a decrease in the minimal effective dose rate for cell kill. Within

the linear quadratic (LQ) model, the best matching *in vivo* survival correlation (α=0.1 Gy^{-1}, α/β=100 Gy, T_μ=60 h, T_D=14.5 d) indicates a relative biological effectiveness value of 0.4 in comparison to EBRT. **Conclusion**: Our results demonstrate that accurate dosimetric modelling is crucial to establish dose-response correlations enabling optimization of treatment protocols.

Key Words: Radiation dosimetry, Dose-effect relationship, Peptide receptor radionuclide therapy, ^{177}Lu-DOTATATE

INTRODUCTION

Targeted radionuclide therapy (TRT) using beta-emitting radiolabeled somatostatin analogues is currently applied in patients bearing inoperable neuroendocrine tumors (NETs) which overexpress the somatostatin receptor type-2 ($SSTR_2$) (*1*). Treatment options include [^{90}Y]Y-DOTA-[Tyr^3]octreotide (^{90}Y-DOTATOC) and [^{177}Lu]Lu-DOTA-[Tyr^3]octreotate (^{177}Lu-DOTATATE) which is registered as Lutathera®.

^{177}Lu-DOTATATE therapy has shown to be successful for many patients, leading to markedly prolonged survival and better quality of life in comparison to other therapies (*2*,*3*). However, ^{177}Lu-DOTATATE therapy is prescribed at a fixed activity dosing scheme primarily irrespective of patient's weight, age, disease burden, uptake and tumor specific radiosensitivity (*4*), leading to a sub-optimal but overall safe therapy.

In addition, preclinical research into TRT has been marked by the scarcity of dosimetric evaluations, sound radiobiological understanding and absorbed dose-effect models that could predict tumor response. In spite of this, evidence strongly implies the existence of an absorbed dose-effect relationship (*5*), which could be used to guide personalized treatment for an optimized therapeutic approach.

Historically, tumor response to TRT has been related to macroscopic quantities such as whole-tumor absorbed dose, assuming uniform distribution of the internalized radionuclide and hence, uniform energy deposition (*6*). However, the biologic response among cells within a tumor can vary greatly, depending on the spatial heterogeneity of dose distributions at multicellular, cellular, and sub-cellular levels (*7*,*8*). The knowledge of individual cellular absorbed doses and dose rates, together with their radiation sensitivity (α, β), sub-lethal damage repair and repopulation

capacity is theoretically indispensable to assess the treatment capability to kill every tumor cell, thus impairing tumor regrowth.

At present, few studies have shown that tumor $SSTR_2$ expression status can be associated with clinical outcome (*9*,*10*) and a more recent study has addressed the correlation between $SSTR_2$ levels and DNA double strand breaks (DSBs) formation at a preclinical level (*11*). Here, we used $SSTR_2$ levels as inputs to model tumor (cancer/healthy cells) and activity heterogeneity at cellular scale. The resulting absorbed dose and dose rate calculations were used to determine absorbed dose-effect relationships on both nano- (DNA DSBs) and macro- (*in vivo* tumorous cell survival) scale.

MATERIALS AND METHODS

The biological experimental data used as input for the dosimetric calculations was part of previous studies carried out at Erasmus MC (*11*) and are briefly summarized in the supplemental materials (*12–17*) accompanying this article. Animal experiments were approved by the Animal Welfare Committee of the Erasmus MC and were conducted in accordance with European guidelines.

Absorbed dose and dose rate distribution maps

$SSTR_2$ expression of NCI-H69 xenografts from mice injected with ^{177}Lu-DOTATATE was assessed by immunofluorescent stainings (*11*). Square tissue sections with 3.2 x 3.2 mm side and resolution of 0.625 μm/pixel from 4 independent mice per time point were used to reconstruct 16 voxelized computational models (heterogeneous tumor cell distribution) and the corresponding 16 voxelized sources (heterogeneous radionuclide distribution) at 4 time points (0, 2, 5 and 11 days),

as described in Supplemental material. The input data for the Monte Carlo (MC) simulations is represented by 507x507x289 voxels of 5.7 x 5.7 x 10 μm size.

The Gate MC toolkit version 9.0 (*18*) was used to perform simulations and score 3 dimensional absorbed dose maps (resolution: 5.7 x 5.7 x 10 μm) within the defined geometry. The average dose was also calculated for tumorous and healthy cells with the DoseByRegion actor (deposited energy per dose voxel mass).

The radioactive source was sampled using the predefined ion source definition (ENSDF database), which includes all the spectral components of ^{177}Lu. The Livermore physics list (low-energy electromagnetic model) with a production cut off for the secondary electron of 1 μm was adopted.

The uncertainty when merging the dose maps computed over different cores was calculated according to Chetty et. al (*19*). The total number of particles was chosen to ensure an average error below 6% for all the simulations.

The biodistribution data (*11*) was used to calculate the effective half-life averaged over the whole sections and thus the cumulated activity. The absorbed dose maps were corrected for the number of particles simulated and the bound fraction of activity over different time points, to determine realistic absorbed dose rate distributions over time.

Dose Volume Histograms (DVH) and generalized Equivalent Uniform Dose (gEUD), as defined in Eq. 1, were calculated using a Python (*12*) application in order to compare the volumetric dose distribution of the heterogeneously distributed radionuclide to the reference case of a uniform spherical source distribution.

The S-value and dose rate distribution calculations for the equivalent uniform spherical phantom were performed on GATE (*18*) using the same physical settings and geometrical volume and then compared to OLINDA (*20*) and IDAC (*21*) codes.

$$gEUD = \left(\frac{1}{N}\sum_{i=1}^{N} d_i^a\right)^{\frac{1}{a}} \quad (1)$$

Where d_i represents the absorbed dose in each tumor cell volume (i.e. voxel) and a is a negative parameter relating the effects by heterogeneous and uniform dose distributions.

In vivo survival model

The efficacy of the heterogeneous absorbed dose distribution caused by the receptor expression pattern compared to an equivalent homogeneous activity distribution (spherical phantom) was investigated by comparing the corresponding *in vivo* survivals. Calculations were performed accounting for the dose rate distribution over the tumor cells (i^{th} voxel) at the time of tissue excision ${R_0}^i$ (Eq. 2, Fig. 1) or by means of average dose rate S-value determined considering the initial SSTR expression status, hereinafter defined as "average" approach.

$$\frac{dD(t)^i}{dt} = \left({R_0}^i - P\right)\exp(-\lambda_e t) + P\ \exp\left(-\lambda_p t\right),\ 0 \le t \le T_j \quad (2)$$

Where P (biological plateau) and λ_e (effective half-life) are parameters obtained by fitting the biodistribution as previously reported (*11*).

$$D(t)^i = \int_{-\infty}^{\infty} dt\, \frac{dD(t)^i}{dt} = \int_0^T dt\, \frac{dD(t)^i}{dt}$$
$$= \left(\frac{{R_0}^i - P}{\lambda_e}\right)(1 - exp\,(-\lambda_e t)\,) + \frac{P}{\lambda_p}\left(1 - exp\,\left(-\lambda_p t\right)\right) \quad (3)$$

$$G(t)^i = \frac{2}{D(t)^2}\left[\frac{({R_0}^i - P)^2}{({\lambda_e}^2 - \mu^2)}\left(1 - e^{-(\lambda_e+\mu)t}\right)\right.$$
$$+ \frac{\left({R_0}^i - P\right)P}{(\lambda_e - \mu)(\lambda_p + \mu)}\left(1 - e^{-(\lambda_p+\mu)t}\right) + \frac{\left({R_0}^i - P\right)^2}{2\lambda_e(\mu - \lambda_e)}\left(1 - e^{-2\lambda_e t}\right)$$
$$- \frac{\left({R_0}^i - P\right)P}{(\lambda_e - \mu)(\lambda_p + \lambda_e)}\left(1 - e^{-(\lambda_p+\lambda_e)t}\right)$$
$$+ \frac{\left({R_0}^i - P\right)P}{(\lambda_p - \mu)(\lambda_e + \mu)}\left(1 - e^{-(\lambda_e+\mu)t}\right) \quad (4)$$
$$+ \frac{P^2}{({\lambda_p}^2 - \mu^2)}\left(1 - e^{-(\lambda_p+\mu)t}\right)$$
$$- \frac{\left({R_0}^i - P\right)P}{(\lambda_p - \mu)(\lambda_e + \lambda_p)}\left(1 - e^{-(\lambda_e+\lambda_p)t}\right)$$
$$\left. + \frac{P^2}{2\lambda_p(\mu - \lambda_p)}\left(1 - e^{-2\lambda_p t}\right)\right]$$

$$E(t)^i = \exp(\gamma t)\ \exp\left(-\alpha D(t)^i - G(t)^i \beta {D(t)^i}^2\right) \quad (5)$$

The dose D(t) and the Lea-Catcheside factor G(t) (Supplemental material), reported in Eq. 3 and 4 respectively, are used to describe the *in vivo* survival E(t) (Eq. 5), according to the linear quadratic (LQ) model (*22*). The repair rate μ in Eq. 4 was evaluated by fitting the available in vitro γH2AX foci data (Supplemental Fig. 1A). E(t) was then corrected for tumor repopulation, with repopulation rate γ, obtained by fitting the tumor growth curve according to Eq. 6 and imposing T_0

(onset of shrinkage) as equal to 3 days (Supplemental Fig. 1B). The regrowth doubling time (T_D) was then calculated as $\frac{ln\,(2)}{k_0-k_1+k_2}$, with k_i indicating growth and shrinkage rates and $\gamma = \ln(2)/ T_D$.

$$V = V_0 \cdot e^{k_0 t} \cdot max_{t>T_0} e^{-k_1(t-T_0)} \cdot max_{t>T_1} e^{k_2(t-T_1)} \quad (6)$$

The cellular radiosensitivity α and β were taken as variable parameters with α 0.264 Gy^{-1}, extracted from low-dose rate (0.002– 0.05 Gy/min) external irradiation data (*23*) or α 0.14 Gy^{-1}, from internal exposure (*24*), and α/β 5, 10 and 100 Gy. The effect of a variable radiation sensitivity among the cell population (biological uncertainty) was tested using the following Gaussian distributions: α 0.264 ± 0.04 Gy^{-1} and 0.14 ± 0.03 Gy^{-1}.

The tissue sections of 4 different mice excised at 0, 2, 5 and 11 days were used to calculate the *in vivo* survival distribution within time each interval T_i (0-2 days, 2-5 days, 5-11 days, 11-14 days). Then, the final survival distribution was obtained by sampling the average survival distribution in each of the previous time interval $E(T_j - 1)$ and statistically adding it to the next one as reported in Eq. 7.

$$E(T_j) = E(T_j - 1) \exp\left(-\alpha D(T_j) - G\beta D(T_j)^2 + \gamma T_j\right) \quad (7)$$

The modelled results were then compared to the terminal deoxynucleotidyl transferase-mediated dUTP nick-end labeling (TUNEL) assay measurements (*11*) corrected for tumor shrinkage after day 4.

Correlation between absorbed dose and DSB level

Using the same methodology outlined before, simulations on smaller tissue sections with higher resolution (320 μm x 320 μm with resolution of 0.325 μm/pixel) co-stained for γHA2X and $SSTR_2$ expression at day 2 were used to seek a correlation with the average absorbed dose delivered

to the tumor cells within these 2 days. High resolution voxelized computational models and sources made of 512 x 512 x 256 voxels with size 0.6 x 0.6 x 1.3 μm were used as input for the dose simulations using GATE.

In addition, we identified areas within the large tissue sections (used for the *in vivo* survival calculations) most likely characterized by high level of DSBs damage by employing a template matching technique (Supplemental material – Supplemental Fig. 2). High expressing $SSTR_2$ cells (with high level of DSBs) in the smaller tissue sections (used for DSB analysis) were used as template. The identified areas, expected to present high level of DSBs damage, were then compared with the absorbed dose delivered over 2 days and the dose rate map at day 2. As such we extended the absorbed dose-to-DSBs correlation, found on the small tissue sections, also over larger volumes.

Statistical analysis

Selection of the most likely curve fitting result to obtain the input parameters of the *in vivo* survival model was performed using the corrected Akaike Information Criterion (AICc). Fitting was performed according to the least square method, with Pearson R^2 as parameter for its goodness ($R^2 \geq 0.7$).

The Shapiro-Wilk test was used for analyzing whether the DSBs data were distributed normally, whilst Q-Q plots verified the normality of dose distributions.

The Paired T-test was used to assess the significant difference ($p<0.05$) between sets of data within the S-value and *in vivo* survival modeling comparison.

RESULTS

Good correlation between absorbed dose and DSBs

The number of DSBs/cell, measured by the total number of γH2AX foci in the smaller co-stained sections (n=8) taken from the 4 tumors (B1-B4 in Supplemental Table 1), ranged from 0.47 to 3.34 per cell. The absorbed dose to the cancer cells ranged from 1637 to 1759 mGy per 30 MBq ^{177}Lu administered. We first fitted the DSBs per cell as a function of the absorbed dose to the cancer cells for each tumor volume separately, verifying a normal distribution for the slopes with the Shapiro-Wilk test ($p=0.49$). The mean value of the slopes was 0.0235 DSB/cell mGy^{-1}. Then, pooling all the data, we found a good correlation with a slope of 0.0223±0.0231 DSBs/cell mGy^{-1} ($R^2=0.7$) (Fig. 2A). For illustrative purpose the graphical correspondence between $SSTR_2$ levels (Fig. 2B), absorbed dose (Fig. 2C) and DSBs induction (Fig. 2D) is highlighted for a representative tile-scan image.

The remaining $SSTR_2$ expression images and absorbed dose maps, from which the average correlation is drawn, are reported in Supplemental Fig. 3.

Using the smaller tissue sections characterized by prevalently high expressing $SSTR_2$ cells and high level of DSB induction (Fig. 3A) as template, we found the location of similar receptor expression patterns in the larger tissue section (Fig. 3B) excised from the same tumor volume (B1-B4) in order to verify the existence of a macroscale correlation. The degree of similarity is indicated by the red-to-yellow color map overlaid on top of the original tissue section image (Fig. 3C). Reporting the corresponding absorbed dose over a 2 day period (Fig. 3D), we can observe that the red areas match the highest absorbed dose regions, indicating again a good macroscale correlation with potentially high DSBs forming areas. Similar template matching results for the 3 remaining tissue samples are reported in Supplemental Fig. 4.

Homogeneous and heterogeneous exposures deliver comparable average absorbed doses

The average absorbed dose delivered to each tissue section after 2, 5, 11 and 14 days is reported in Supplemental Table 1 in comparison with the corresponding homogeneous spherical

exposure. The excised tissue sections are mostly made of tumor cells (94% - 100%), similarly to the spherical homogenous calculations, in which the volume is assumed to be 100% tumorous. Within 2 days, 40% of the dose is delivered to the tumor cells whilst the successive time intervals contribute in the same percentage (about 20%) to the total absorbed dose.

The homogeneous spherical S-value is 8.71E-10 Gy/decay, 8.90E-10 Gy/decay and 8.94E-10 Gy/decay using OLINDA, IDAC and GATE, respectively. It differs significantly from the heterogeneous S-values with the latter being between 2% and 59% higher ($\frac{S_{het}-S_{hom}}{S_{hom}}$) than the homogenous one. In addition, the heterogeneous S-values increase on average over time and the variability among them is up to 62%.

The absorbed dose distributions corresponding to the two exposure types, reported by means of dose and dose rate maps, frequency DVH, cumulative DVH and gEUD in Supplemental Fig. 5 and Supplemental Table 2, are significantly different from each other, given that only the heterogeneous one is normally distributed as shown by the corresponding Q-Q plots. The cumulative DVHs indicate that on average (49.17±3.72)% of the volume is exposed to a dose equal or higher than the average dose for the heterogeneous case compared to 64.46% corresponding to the homogeneous case. Hence, the heterogeneous dose distribution is better represented by its mean value compared to the homogeneous dose distribution, in view of its Gaussian-like behavior. Indeed, the homogeneous absorbed dose distribution over the spherical volume is heavy tailed and negatively skewed because of geometrical reasons.

Nevertheless, on average the absorbed dose characterizing the heterogeneous exposure is not significantly different from the uniform exposure, diverging prominently only after 5 days.

Dose heterogeneity causes significant variation in the treatment outcome

The modeled *in vivo* survival results corresponding to α 0.14 Gy^{-1} (constant), α/β 100 Gy, T_μ 60 h and T_D 14.5 days are shown in Fig. 4. The box-plot distributions corresponding to the remaining radiosensitivity parameters are reported in Supplemental Fig. 6.

No significant difference in survival between the heterogeneous and homogeneous exposure is observed in the first 5 days, when 61% of the radiation dose is delivered. However, in the following days the difference becomes significant with the heterogeneous dose delivery being more effective (higher cell killing) to prevent tumor regrowth.

Interestingly, the heterogeneous dose rate distribution among the cell population causes a significant dispersion and hence uncertainty in the treatment outcome due to solely physical parameters.

Hypothesizing a Gaussian distribution of the radiation sensitivity (α) to account for a realistic tumor heterogeneity, causes the standard deviation for cell survival to be so large that the treatment outcome would be likely unpredictable (Supplemental Fig. 7).

Averaging the results for the tissue sections belonging to the same time group, we obtained the distribution in Fig. 5A, where the constant α and α/β ratios are used as variable parameters. As expected, the higher the α the more the cell killing for a given dose, whilst a higher α/β ratio reduces the cell killing by multi hits. Compared to the experimental TUNEL assay results, corrected for the clearance estimated with the tumor growth curve after day 4 (Fig. 5B), the results for α 0.14 Gy^{-1} and α/β 100 Gy match well the experimental cell death within the radiobiological uncertainties.

The *in vivo* survival correlation calculated with the average approach (α =0.1 Gy^{-1}, α/β =100 Gy, T_μ = 60 h, T_D=14.5d) is then reported with the experimental tumor volume data shifting the onset of volume reduction to account for the delay caused by the removal of dead cells (Fig. 5C).

The *in vivo* results corresponding to the heterogeneous exposure (Gaussian distributed α) and the uniform exposure are reported in Supplemental Fig. 8.

DISCUSSION

Integrating radiobiological knowledge into the decision-making process at clinical level is of uttermost importance to optimize the therapeutic use of radionuclides. Here, micro-scale dose assessments based on $SSTR_2$ expression pattern from excised tissue sections reveal a good correlation between absorbed dose and DSBs induction and a resulting *in vivo* cell death model that well match the experimental results.

Recently, it was shown that $SSTR_2$ expression levels correlate with DSBs induction after ^{177}Lu-DOTATATE treatment for NCI-H69 xenografts (*11*). Similarly, a qualitative analysis revealed that ^{177}Lu uptake correlates with γH2AX focus induction for CA209478 xenografts (*25*). The same applies at clinical level, where high $SSTR_2$ expression was associated with longer overall and progression free survival (*9*,*10*). However, in all the aforementioned studies an absorbed dose-DSBs correlation, following accurate absorbed dose calculations, was not investigated. At present, only few studies tried to correlate the absorbed dose with DNA damage after ^{177}Lu-DOTATATE treatment (*26*,*27*). In this respect, Denoyer et al. (*26*) failed to prove the existence of a correlation between the absorbed dose to blood or spleen and the induction of γH2AX foci in peripheral blood lymphocytes of 11 patients undergoing peptide receptor radionuclide therapy (PRRT) while finding a poor correlation for bone marrow and tumor. Arguably, the reason may lie in the application of general macro-dosimetric modelling (MIRD method at organ level), and hence, unavailability of specific dosimetry at functional cell level. Conversely, Eberlein et al. (*27*) found a linear relationship between the number of DSBs foci per cell, measured by the co-localized biomarkers γH2AX and 53BP1, and the absorbed dose to the blood. In comparison with our study, we found a

1.5 times higher number of DSBs foci per cell per mGy . One reason could be the presence of specific uptake in tumor cells, although the absorbed dose should form an independent parameter. Most probably, the simplified dosimetric modeling causes this difference as well. Indeed, it was demonstrated previously (*28*) that accounting for a realistic distribution of vessel sizes results in absorbed dose estimations lower than the maximum energy deposited by beta particles.

Unlike these studies, our methodology allowed to investigate the micro-scale dose distribution over functional volumes (i.e. tumor cells) finding significant differences between homogeneous and heterogeneous dose distributions over the tumor volume. Nonetheless, the heterogeneous dose delivery proved to be as effective as the homogeneous one, possibly due to the long range of ^{177}Lu-beta particles. In this respect, however, it is important to highlight that H69 tumor model is most probably more homogeneous in its receptor expression than actual pancreatic and SI NET tumors. Furthermore, the growing interest in short range radionuclides for TRT will increase the impact of heterogeneity as well, making refined dosimetry methods indispensable. For this reason, a thorough investigation on the $SSTR_2$ expression in 3 dimensions and over time, would help further characterizing the DNA damage induction.

Accurate dose rate calculation is essential to determine cell death caused by PRRT as well, since during protracted exposure at relatively low dose rates, induction of DNA lesions competes with DNA damage repair, reducing the cell killing. Our radiosensitivity parameter analysis for the *in vivo* survival correlation indicates that the minimal effective dose rates for cell kill corresponding to α/β =100 Gy are 13.72 mGy/h and 7.40 mGy/h, with α = 0.14 Gy^{-1} and 0.264 Gy^{-1}, respectively. Moreover, a lower α/β leads to a decrease in the minimal effective dose rate for cell kill.

Certainly, besides accurate absorbed dose rate calculations, radiobiological modelling based on the LQ model requires specific knowledge of the radiosensitivity parameters (α, β and T_μ). Our study, in agreement with our previous findings (*29*), demonstrate that extrapolating these

parameters from external beam radiotherapy (EBRT) may not be representative of ^{177}Lu-DOTATATE therapy, since they do not account for the intrinsic cellular response to ^{177}Lu β-particles. Strikingly, the volume response as a function of time best matched the experimental result with an alpha value of 0.1 Gy^{-1}, indicating a relative biological effectiveness (RBE) of 0.4 in comparison to EBRT (α = 0.264 Gy^{-1}). Derivation of the relative biological effectiveness was performed as indicated for alpha-particle response (*30*) since the quadratic term could be neglected, despite the long DNA damage repair half-life of 60 h, experimentally determined. Hence, focusing on the difference in radiation sensitivity parameter α between internal and external exposures, our finding resembles the difference reported by Lee et al. (*31*), between ^{90}Y and external beam exposure of DLD-1 colorectal cancer cells (RBE_{MAX} = 0.4).

In addition, our methodology does take into account the potential tumor sensitivity heterogeneity assuming a probabilistic distribution (Gaussian) of the α value, which combined with the heterogeneous dose rate distribution at microscale level, could lead to an unpredictable treatment outcome (*32*). However, we did not account for any cell cycle-related change, which might be relevant to include in future models, because the fraction of cells in a specific sensitive or radioresistant phase could gradually increase during protracted irradiation (*33*,*34*) leading to a specific radio-sensitivity distribution among the cell population. In view of this, sub-lethal damage repair would vary depending on the dose rate, and the LQ model would not be adequate to describe the tumor response.

More studies investigating the temporal variation of dose rates over time against biological phenomena such as DNA repair capacity, cell cycle progression and proliferation over the cell population would help to better understand the underlying biological mechanisms of TRT to further improve biophysical modeling.

To conclude, it must be noted that this work is purely a radiobiology modelling study, for which the small cell lung cancer NCI-H69 cell line was the most appropriate choice since it is (1) well established, in contrast to experimental models for gastroenteropancreatic neuroendocrine tumor (GEPNET); (2) largely used for PRRT studies (*35*); (3) classified as pulmonary NET (*36*); (4) expressing neuroendocrine markers, such as chromogranin A, synaptophysin, neuron-specific enolase (NSE), protein gene product (PGP) 9.5 and $SSTR_2$, and hence demonstrating its neuroendocrine phenotype and overall usefulness as model for studying SSTR-TRT in NETs (*37*). Approximations and model parameters limit the presented correlation to this specific pre-clinical setting. Indeed, higher proliferation rate and homogeneity characterizing available pre-clinical therapy models, may lead to dose overestimations or an incorrect definition of therapy cycles, if the results would be extrapolated to clinics, especially for larger tumor volumes. A further step would consist in investigating cell models more representative of NET tumors in humans, possibly transplanting them from patients into mice (*38*) and, as such, including tumor microenvironmental parameters as hypoxia and immune-system effects, in order to increase the translational power of biophysical models.

CONCLUSION

In this study we developed a methodology to understand and further improve the absorbed dose characterization for PRRT during *in vivo* experiments by using the $SSTR_2$ expression of tumor xenografts. Adopting this methodology, a clear correlation between the absorbed dose and the average number of DSBs per cell after ^{177}Lu-DOTATATE exposure has been established. Furthermore, we investigated the radiosensitivity parameters of NCI-H69 cells, concluding that the α-value for cells exposed to ^{177}Lu-DOTATATE is significantly different from EBRT.

DISCLOSURE

No conflicts of interest exist.

KEY POINTS

QUESTION: Can dose-effect relationships for DSBs and tumor volume reduction be established for *in vivo* ^{177}Lu-DOTATATE experiments?

PERTINENT FINDINGS: Through accurate dosimetric modelling, a good (R^2=0.7) linear correlation (slope of 0.022±0.0231 DSBs/cell mGy^{-1}) between the absorbed dose and the average number of DSBs per cell after ^{177}Lu-DOTATATE exposure has been established. Furthermore, the α-value for cells exposed to ^{177}Lu-DOTATATE is significantly different from that derived after external beam exposure.

IMPLICATIONS FOR PATIENT CARE: Distinct differences were found between the cellular dose and the average tumor dose, which might impact clinical tumor dosimetry evaluation for targeted therapy.

REFERENCES

1. Nicolas GP, Morgenstern A, Schottelius M, Fani M. New developments in peptide receptor radionuclide therapy. *J Nucl Med*. 2019;60:167-171.

2. Strosberg J, Wolin EM, Chasen B, et al. Improved time to quality of life deterioration in patients with progressive midgut neuroendocrine tumors treated with 177Lu-DOTATATE: the NETTER-1 phase III trial. *Ann Oncol*. 2017;28(suppl 5):146.

3. Strosberg J, El-Haddad G, Wolin E, et al. Phase 3 trial of 177Lu- DOTATATE for midgut neuroendocrine tumors. *N Engl J Med*. 2017;376:125-135.

4. Hope TA, Abbott A, Colucci K, et al. NANETS/SNMMI procedure standard for somatostatin receptor-based peptide receptor radionuclide therapy with 177Lu-DOTATATE. *J Nucl Med*. 2019;60:937-943.

5. Strigari L, Konijnenberg M, Chiesa C, et al. The evidence base for the use of internal dosimetry in the clinical practice of molecular radiotherapy. *Eur J Nucl Med Mol Imaging*. 2014;41:1976-1988.

6. Zanzonico PB. Internal radionuclide radiation dosimetry: a review of basic concepts and recent developments. *J Nucl Med*. 2000;41:297-308.

7. O'Donoghue JA. Implications of nonuniform tumor doses for radioimmunotherapy. *J Nucl Med*. 1999;40:1337-1341.

8. Neti PVSV, Howell RW. When may a nonuniform distribution of 131I be considered uniform? An experimental basis for multicellular dosimetry. *J Nucl Med*. 2003;44:2019-2026.

9. Mehta S, De Reuver PR, Gill P, et al. Somatostatin receptor SSTR-2a expression is a stronger predictor for survival than Ki-67 in pancreatic neuroendocrine tumors. *Medicine(Baltimore)*. 2015;94:e1281.

10. Qian ZR, Li T, Ter-Minassian M, et al. Association between somatostatin receptor expression and clinical outcomes in neuroendocrine tumors. *Pancreas*. 2016;45:1386-1393.

11. Feijtel D, Doeswijk GN, Verkaik NS, et al. Inter and intra-tumor somatostatin receptor 2 heterogeneity influences peptide receptor radionuclide therapy response. *Theranostics*. 2020;11:491-505.

12. Python Software Foundation. Python Language Reference, version 3.6.3.

13. Peng T, Thorn K, Schroeder T, et al. A BaSiC tool for background and shading correction of optical microscopy images. *Nat Commun*. 2017;8:1-7.

14. White DR, Griffith R V, Wilson IJ. Report 46. *J Int Comm Radiat Units Meas*. 1992;os24:11.

15. Perreault S, Hébert P. Median filtering in constant time. *IEEE Trans Image Process*. 2007;16:2389-2394.

16. Porikli F. Integral histogram: a fast way to extract histograms in Cartesian spaces. In: 2005 IEEE Computer Society Conference on Computer Vision and Pattern Recognition (CVPR'05). 2005;1:829-836.

17. Nonnekens J, van Kranenburg M, Beerens CE, et al. Potentiation of peptide receptor radionuclide therapy by the PARP Inhibitor Olaparib. *Theranostics*. 2016; 6: 1821-32

18. Jan S, Santin G, Strul D, et al. GATE: a simulation toolkit for PET and SPECT. *Phys Med*

Biol. 2004;49:4543-4561.

19. Chetty IJ, Rosu M, Kessler ML, et al. Reporting and analyzing statistical uncertainties in Monte Carlo-based treatment planning. *Int J Radiat Oncol Biol Phys*. 2006;65:1249-1259.

20. Stabin MG, Sparks RB, Crowe E. OLINDA/EXM: the second-generation personal computer software for internal dose assessment in nuclear medicine. *J Nucl Med*. 2005;46:1023-1027.

21. Andersson M, Johansson L, Eckerman K, Mattsson S. IDAC-Dose 2.1, an internal dosimetry program for diagnostic nuclear medicine based on the ICRP adult reference voxel phantoms. *EJNMMI Res*. 2017;7:88.

22. Solanki JH, Tritt T, Pasternack JB, et al. Cellular response to exponentially increasing and decreasing dose rates: implications for treatment planning in targeted radionuclide therapy. *Radiat Res*. 2017;188:221-234.

23. Björk-Eriksson T, West C, Karlsson E, Mercke C. Discrimination of human tumor radioresponsiveness using low-dose rate irradiation. *Int J Radiat Oncol Biol Phys*. 1998;42:1147-1153.

24. Konijnenberg M, Bison S, Santini C, Melis M, de Blois E, De Jong M. Treatment planning options for 177Lu-DOTA, Tyr3-octreotate; verification of therapeutic dose-responses in an animal model. *J Nucl Med*. 2018;59(suppl 1):318.

25. O'Neill E, Kersemans V, Allen PD, et al. Imaging DNA damage repair in vivo after 177Lu-DOTATATE therapy. *J Nucl Med*. 2020;61:743-750.

26. Denoyer D, Lobachevsky P, Jackson P, Thompson M, Martin OA, Hicks RJ. Analysis of 177Lu-DOTA-octreotate therapy-induced DNA damage in peripheral blood lymphocytes of

patients with neuroendocrine tumors. *J Nucl Med*. 2015;56:505-511.

27. Eberlein U, Peper M, Fernández M, Lassmann M, Scherthan H. Calibration of the γ-H2AX DNA double strand break focus assay for internal radiation exposure of blood lymphocytes. *PLoS One*. 2015;10:e0123174.

28. Hänscheid H, Fernández M, Lassmann M. The absorbed dose to blood from blood-borne activity. *Phys Med Biol*. 2015;60:741-753.

29. Tamborino G, De Saint-Hubert M, Struelens L, et al. Cellular dosimetry of [177Lu]Lu-DOTA-[Tyr3]octreotate radionuclide therapy: the impact of modeling assumptions on the correlation with in vitro cytotoxicity. *EJNMMI Phys*. 2020;7:8.

30. Hobbs RF, Howell RW, Song H, Baechler S, Sgouros G. Redefining relative biological effectiveness in the context of the EQDX formalism: implications for alpha-particle emitter therapy. *Radiat Res*. 2014;181:90-98.

31. Lee BQ, Abbott EM, Able S, et al. Radiosensitivity of colorectal cancer to (90)Y and the radiobiological implications for radioembolisation therapy. *Phys Med Biol*. 2019;64:135018.

32. Buffa FM, Nahum AE. Monte Carlo dose calculations and radiobiological modelling: analysis of the effect of the statistical noise of the dose distribution on the probability of tumour control. *Phys Med Biol*. 2000;45:3009-3023.

33. Yong KJ, Milenic DE, Baidoo KE, Brechbiel MW. 212Pb-radioimmunotherapy induces G2 cell-cycle arrest and delays DNA damage repair in tumor xenografts in a model for disseminated intraperitoneal disease. *Mol Cancer Ther*. 2012;11:639-648.

34. Graf F, Fahrer J, Maus S, et al. DNA double strand breaks as predictor of efficacy of the alpha-particle emitter Ac-225 and the electron emitter Lu-177 for somatostatin receptor targeted radiotherapy. *PLoS One*. 2014;9:e88239.

35. Schmitt A, Bernhardt P, Nilsson O, et al. Biodistribution and dosimetry of 177Lu-labeled [DOTA 0,Tyr3]octreotate in male nude mice with human small cell lung cancer. *Cancer Biother Radiopharm*. 2003;18:593-599.

36. Travis WD, Brambilla E, Nicholson AG, et al. The 2015 World Health Organization classification of lung tumors: impact of genetic, clinical and radiologic advances since the 2004 classification. *J Thorac Oncol*. 2015;10:1243-1260.

37. Reubi JC, Waser B, Sheppard M, Macaulay V. Somatostatin receptors are present in small-cell but not in non-small-cell primary lung carcinomas: relationship to EGF-receptors. *Int J Cancer*. 1990;45:269-274.

38. De Jong M, Maina T. Of mice and humans: are they the same? - Implications in cancer translational research. *J Nucl Med*. 2010;51:501-504

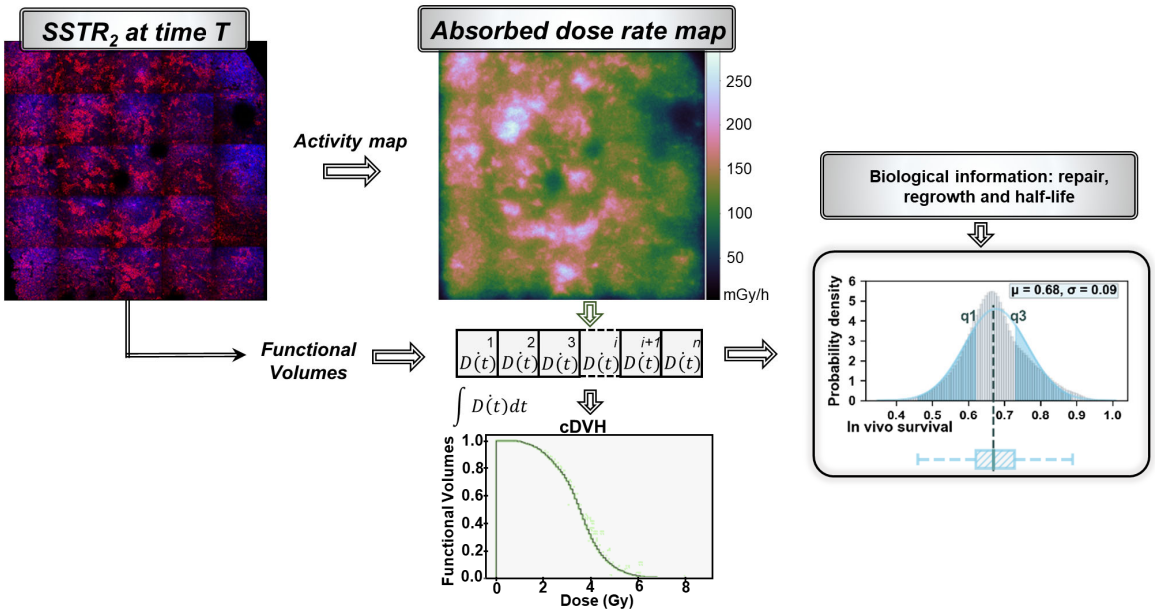

FIGURE 1. Schematic representation of the methodology used to model the *in vivo* survival distribution starting from the immunofluorescent $SSTR_2$ stainings used to define the activity map (source) and the functional volumes (tumor cells). The dose rate in each tumor voxel and the radiobiological information are then integrated in the LQ model to evaluate the *in vivo* survival distribution within time intervals $E(T_i)$. The probability density function of the survival (light grey histogram) is approximated by a Gaussian distribution (light blue) and reported with box-plots to simplify the representation. The volumetric absorbed dose computed over the tumor cells is alternatively reported in 2D by means of cumulative DVH (cDVH).

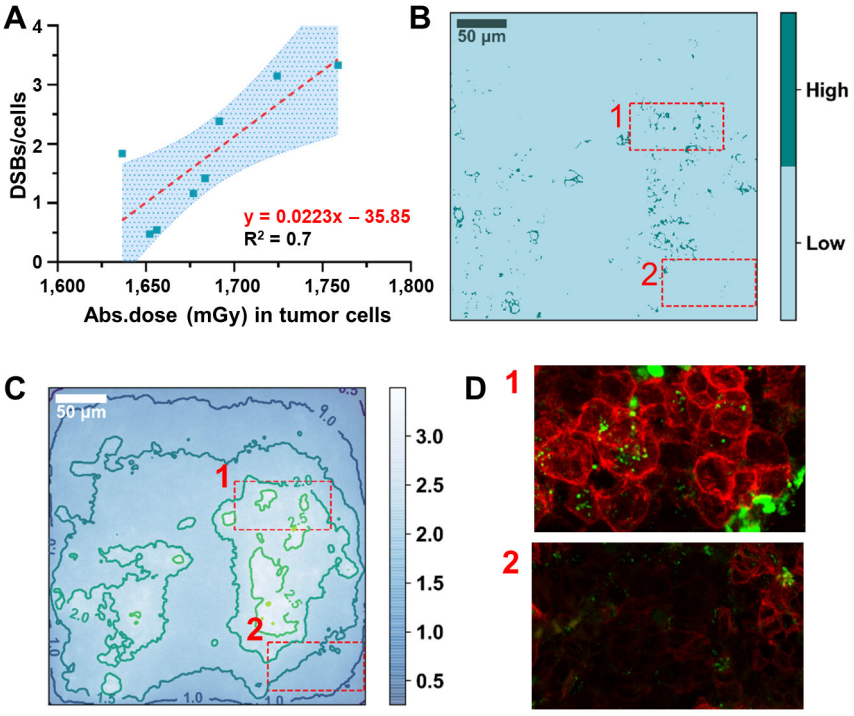

FIGURE 2. Absorbed dose-response. (A) Correlation between average absorbed dose delivered to cancer cells and total number of DSBs measured by γHA2X foci formation. The highlighted area indicates the 95% confidence interval. (B) Representative tile-scan of $SSTR_2$ stainings thresholded to identify low- (light blue) and high- (green) $SSTR_2$ expressing areas. (C) Absorbed dose distribution map contoured for iso-dose levels with color bar in Gy. (D) Zoom of $SSTR_2$ (red) and γH2AX (green) immunofluorescent stainings corresponding to high- and low- level of $SSTR_2$ expression, indicated by 1 and 2, respectively.

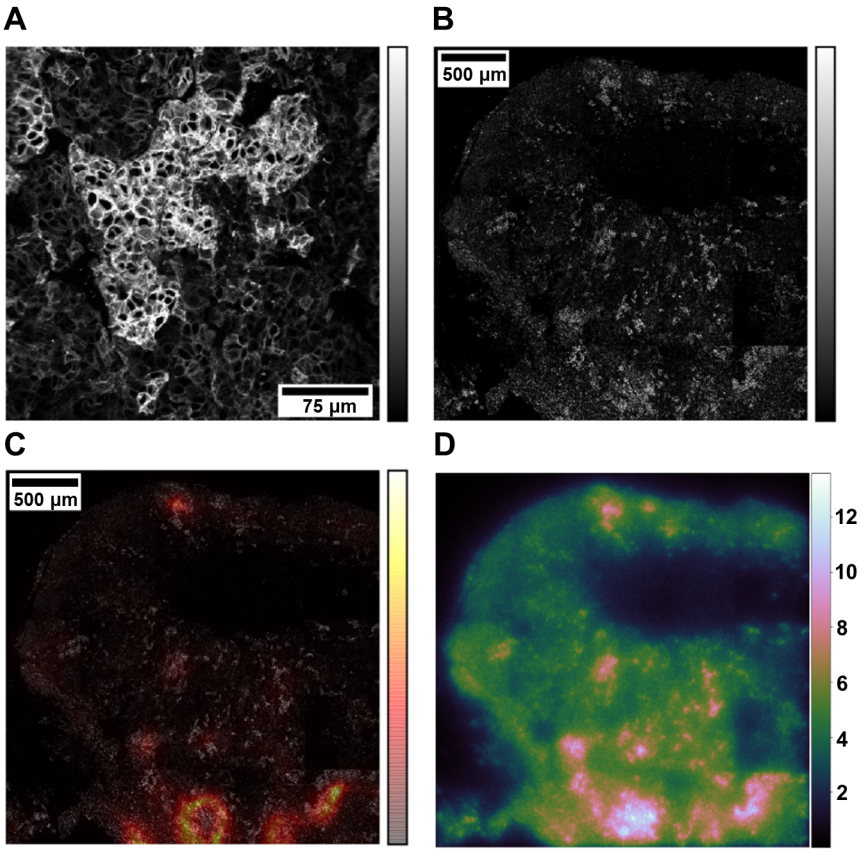

FIGURE 3. Template matching technique. (A) Small tissue section used as template. (B) Large tissue section used as "test image". (C) Color map indicating the similarity score based on the χ^2 value overlaid on top of the large tissue section. Color bars indicate the pixel intensities of the tile-scans (greyscale) or similarity map (red-yellow). (D) Absorbed dose map with color bar in Gy.

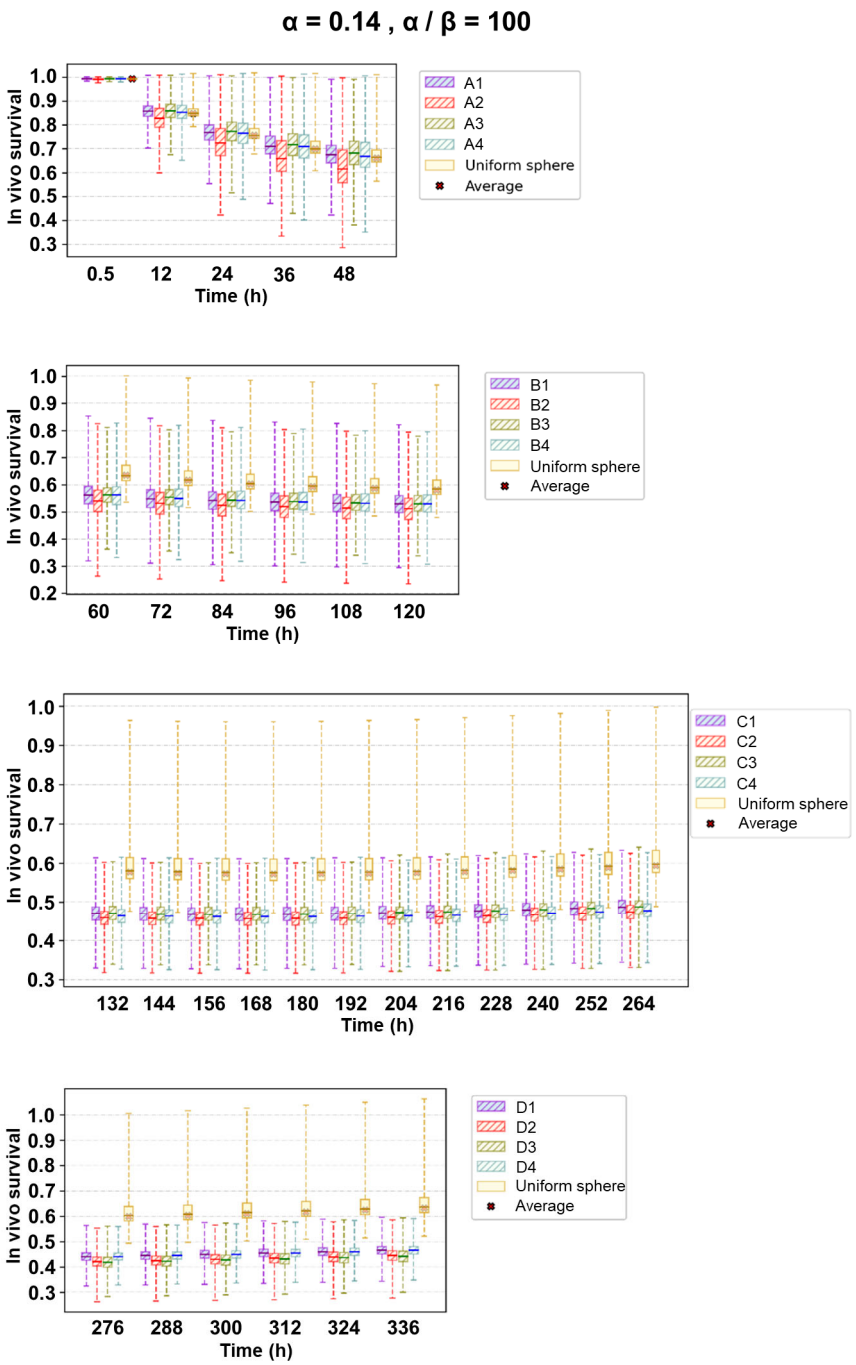

FIGURE 4. Box plots indicating the *in vivo* survival distribution over time on different excised tissue sections. The whiskers correspond to 1.5 times the interquartile range. The corresponding tissue section nomenclature is reported in Supplemental Table 1.

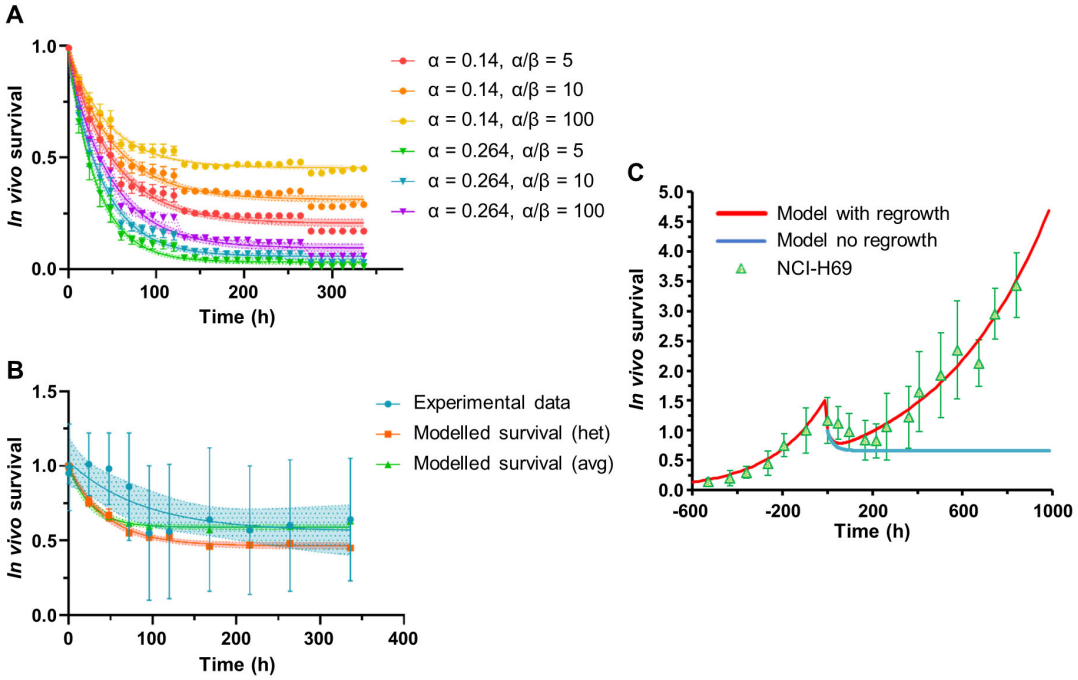

FIGURE 5. *In vivo* survival correlations. (A) Radiosensitivity parameter analysis for the modelled heterogeneous survival (het). (B) Comparison with experimental data (TUNEL assay; 0h = time of injection), including the modelled results for the average approach (avg) (i.e. one average S-value). The error bars indicate 1 SD. (C) Cell survival correlation with (red) and without regrowth (blue) for the average calculation approach together with the fitted relative tumor volume (0h = onset of shrinkage shifted of 3 days) curve normalized to the volume at time of injection (green triangles).

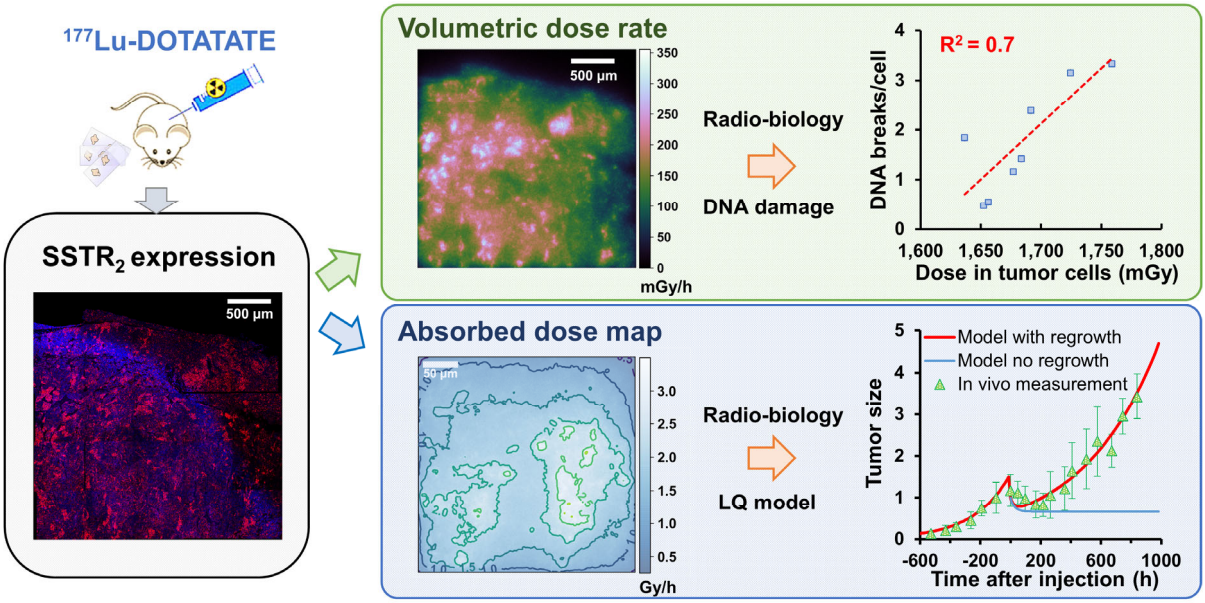
177Lu-DOTATATE
SSTR2 expression
500 µm
Volumetric dose rate
500 µm
350
300
250
200
150
100
50
0
mGy/h
Radio-biology
DNA damage
DNA breaks/cell
R2 = 0.7
4
3
2
1
0
1,600 1,650 1,700 1,750 1,800
Dose in tumor cells (mGy)
Absorbed dose map
3.0
2.5
2.0
1.5
1.0
0.5
Gy/h
Radio-biology
LQ model
Tumor size
Model with regrowth
Model no regrowth
In vivo measurement
5
4
3
2
1
0
-600 -200 200 600 1000
Time after injection (h)

Radiobiological experiments for tumor volume response correlation

BALB-c/nude mice were engrafted subcutaneously with 5 x 10^6 NCI-H69 cells and at a tumor size of 369 ± 203 mm^3 mice were injected intravenously with 30 MBq [^{177}Lu]Lu-DOTATATE (n = 4 per group).
Mice were sacrificed and analyzed at 1 h, 1, 2, 3, 4, 5, 7, 9, 11 and 14 days post injection (p.i.). Organs were put in a gamma-counter for measurement of radioactive uptake and then fixed and embedded in paraffin for later analysis. Uninjected animals were used as control (n = 4).
The biodistribution data from the gamma-counter were analyzed to determine the kinetics of the tumors. The measured activity data as a function of time were fitted with single exponential curves, as indicated by (corrected) Akaike's information criterion, using the least-square regression method.
The cells were immunofluorescent (IF) stained as previously described (6). For the stainings p53 binding protein 1 (53BP1) (Novus Biologicals, NB100-904; 1:500), phosphorylated histone 2AX (γH2AX) (Millipore, JBW301; 1:250), $SSTR_2$ (Abcam, 134152; 1:100) primary antibodies were used. Secondary antibodies used are donkey-anti-rabbit IgG Alexa Fluor 594 (Thermo Fisher, A-11078; 1:500) and donkey-anti-mouse IgG Alexa Fluor 488 (Thermo Fisher; A-11005; 1:500).
Tissue sections of 4 μm were deparaffinized and rehydrated. TUNEL assay was performed using the In Situ Cell Death Detection Kit, Fluorescein (Roche, 11684795910) according to manufacturer's instructions.
In order to analyze tumor growth, another set of BALB-c/nude mice were engrafted subcutaneously with 5 x 10^6 NCI-H69 (n = 8) and injected when tumor volumes reached 697 ± 256 mm^3. The treated group was compared to vehicle injected counterparts (n = 8). Tumor volumes were measured three times per week p.i. Mice were sacrificed when tumor volumes reached the humane endpoint of 2000 mm^3.

Radiobiological experiments for double strand breaks (DSBs) correlation

53BP1 and γH2AX focus formation was imaged with a confocal microscope using Z-stack acquisition. ImageJ was utilized to apply the same local threshold (default for DAPI, MaxEntropy for $SSTR_2$) to all images in order to segment nuclei or quantify DAPI signal and quantify IF signal. Foci were quantified using the Find Maxima function.

G factor derivation

$$G(t) = \frac{2}{D^2}\int_{-\infty}^{\infty} dt\ \frac{dD(t)}{dt}\int_{-\infty}^{t} dt'\ \frac{dD(t')}{dt'}\, e^{-\mu(t-t')}$$

Substituting the dose-rate definition and re-ordering:

$$G(t) = \frac{2}{D(t)^2}\int_0^T dt\ \Big((R_0 - P)e^{(-\lambda_b t)} + P\Big)e^{(-\lambda_p t)}\int_{-\infty}^{t} dt'\ \Big((R_0 - P)e^{(-\lambda_b t')} + P\Big)e^{(-\lambda_p t')}\ e^{-\mu(t-t')}$$
$$= \frac{2}{D^2}\int_0^T dt\ \Big((R_0 - P)e^{-(\lambda_e+\mu)t} + Pe^{-(\lambda_p+\mu)t}\Big)\int_{-\infty}^{t} dt'\ \Big((R_0 - P)e^{(-\lambda_e+\mu)t'} + Pe^{(-\lambda_p+\mu)t'}\Big) =$$

Solving the integral in t':

$$G(t) = \frac{2}{D(t)^2}\int_0^T dt\ \Big((R_0 - P) * e^{-(\lambda_e+\mu)t} + Pe^{-(\lambda_p+\mu)t}\Big)\left(\frac{R_0 - P}{\lambda_e - \mu} - \frac{R_0 - P}{\lambda_e - \mu}\ e^{-(\lambda_e-\mu)t} + \frac{P}{\lambda_p - \mu} - \frac{P}{\lambda_p - \mu}e^{-(\lambda_p-\mu)t}\right) =$$

Using linearity and multiplying:

$$G(t) = \frac{2}{D(t)^2}\int_0^T dt\ \left(\frac{(R_0 - P)^2}{\lambda_e - \mu}\ e^{-(\lambda_e+\mu)t} + \frac{(R_0 - P)P}{\lambda_e - \mu}\ e^{-(\lambda_p+\mu)t} - \frac{(R_0 - P)^2}{\lambda_e - \mu}\ e^{-2\lambda_e t} - \frac{(R_0 - P)P}{\lambda_e - \mu}\ e^{-(\lambda_p+\lambda_e)t} + \frac{(R_0 - P)P}{\lambda_p - \mu}\ e^{-(\lambda_e+\mu)t} + \frac{P^2}{\lambda_p - \mu}\ e^{-(\lambda_p+\mu)t} - \frac{(R_0 - P)P}{\lambda_p - \mu}\ e^{-(\lambda_e+\lambda_p)t} - \frac{P^2}{\lambda_p - \mu}\ e^{-2\lambda_p t}\right) =$$

Solving in t:

$$G(t) = \frac{2}{D(t)^2}\left[\frac{(R_0-P)^2}{({\lambda_e}^2-\mu^2)}\left(1 - e^{-(\lambda_e+\mu)t}\right) + \frac{(R_0-P)P}{(\lambda_e-\mu)(\lambda_p+\mu)}\left(1 - e^{-(\lambda_p+\mu)t}\right) + \frac{(R_0-P)^2}{2\lambda_e(\mu-\lambda_e)}\left(1 - e^{-2\lambda_e t}\right) - \frac{(R_0-P)P}{(\lambda_e-\mu)(\lambda_p+\lambda_e)}\left(1 - e^{-(\lambda_p+\lambda_e)t}\right) + \frac{(R_0-P)P}{(\lambda_p-\mu)(\lambda_e+\mu)}\left(1 - e^{-(\lambda_e+\mu)t}\right) + \frac{P^2}{({\lambda_p}^2-\mu^2)}\left(1 - e^{-(\lambda_p+\mu)t}\right) - \frac{(R_0-P)P}{(\lambda_p-\mu)(\lambda_e+\lambda_p)}\left(1 - e^{-(\lambda_e+\lambda_p)t}\right) + \frac{P^2}{2\lambda_p(\mu-\lambda_p)}\left(1 - e^{-2\lambda_p t}\right)\right] \quad \text{and}$$

$$D(t) = \frac{R_0 - P}{\lambda_e}\left(1 - e^{-\lambda_e t}\right) + \frac{P}{\lambda_p}\left(1 - e^{-\lambda_p t}\right)$$

MC input data

Each of the excised tissue section is made of 25 tiles of 640.17x 640.17 μm side. The following steps were implemented in a Python (*1*) program to create, using the ITK (www.itk.org) module, the mhd image file format for the MC input data, i.e. voxelized sources and computational models:

- Crop a 50 pixel frame in each tile to avoid corrections compensating for the vignetting effectjnm (*2*)
- Stitch the 25 tiles together to create a larger tissue section of 3.2 x 3.2 mm side

- Decrease the resolution by means of Lancosz filter
- Create a montage replicating the tissue sections from the previous step
- Apply a low threshold only to the voxelized computational models to discern between tumor cells region (referred to as tumor cells) and remaining healthy tissue (referred to as healthy cells)
- Convert image files into the aforementioned mhd format

The voxelized source is interpreted as a map of emission probabilities for the chosen radionuclide, via a linear translation of each voxel value. The composition of the tumor cell region of the voxelized phantom was defined as in the ICRU Report 46 (*3*), whilst the healthy tissue composition was that of water.

Simulations were carried out on the Dutch national e-infrastructure with the support of SURF Cooperative (4 × 8-core 2.7 GHz Intel Xeon E5-4650 CPUs/node and 256 GB/node), due to the memory requirement of these calculations.

Template matching

First, the templates and large images were modified to have the same resolution of 0.625 μm/pixel. Then, we adopted a sliding window algorithm computing normalized pixel value histograms in regions sized as the template for each pixel belonging to the test image (*4*,*5*). The similarity between the local histograms within the large image (test image) and the template image was computed through a chi-squared based distance metric (Supplemental Figure 2) and displayed with a color map.

The marked matching areas were used to identify the areas most likely to present high level of DSB damage for comparison with absorbed dose (0-2days) and dose rate maps at day 2.

REFERENCES

1. Python Software Foundation. Python Language Reference, version 3.6.3.

2. Peng T, Thorn K, Schroeder T, et al. A BaSiC tool for background and shading correction of optical microscopy images. *Nat Commun*. 2017;8:1-7.

3. White DR, Griffith R V., Wilson IJ. ICRU Report 46: Photon, Electron, Proton and Neutron Interaction Data for Body Tissues.; 1992.

4. Perreault S, Hébert P. Median filtering in constant time. *IEEE Trans Image Process*. 2007;16:2389-2394.

5. Porikli F. Integral histogram: a fast way to extract histograms in Cartesian spaces. *Proc - 2005 IEEE Comput Soc Conf Comput Vis Pattern Recognition*, CVPR 2005. 2005;I:829-837.

6. Nonnekens J, van Kranenburg M, Beerens CE, et al. Potentiation of peptide receptor radionuclide therapy by the PARP Inhibitor Olaparib. *Theranostics*. 2016; 6: 1821-32

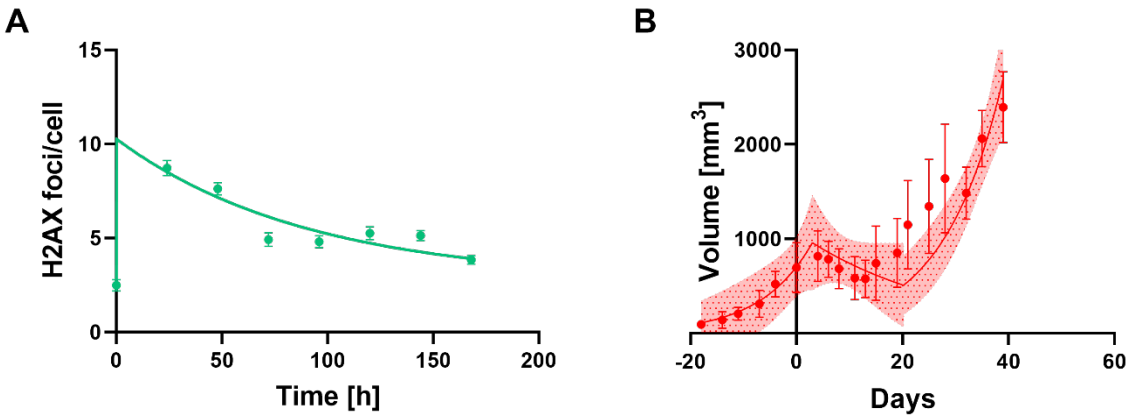

SUPPLEMENTAL FIGURE 1. Experimental radiobiological parameters (11). (2A) *In vitro* quantification of γH2AX foci/cell over time to determine repair rate. The error bars indicate standard error of the mean (SEM). (2B) Tumor growth curve to determine repopulation rate. The error bars indicate 1 standard deviation (SD).

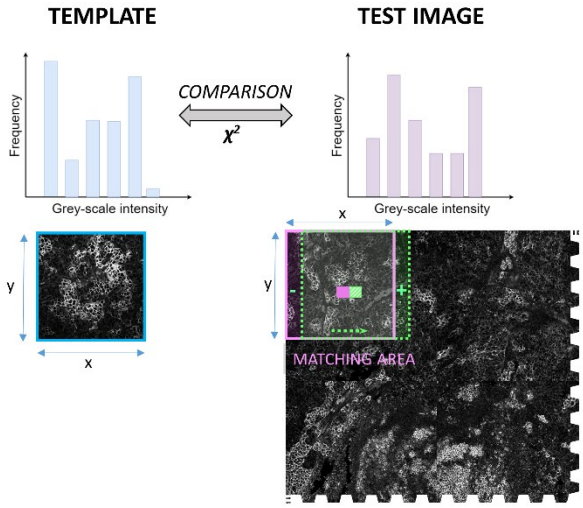

SUPPLEMENTAL FIGURE 2. Schematic representation of template matching algorithm. The template histogram is indicated in light blue, whilst the histogram of the current window centered on the analyzed pixel is indicated in purple. An example of the window movement (towards the right) is shown in green. The window will slide over all the pixels composing the test image and register their similarity score (χ2).

Tissue section B1 “high” $SSTR_2$ expression

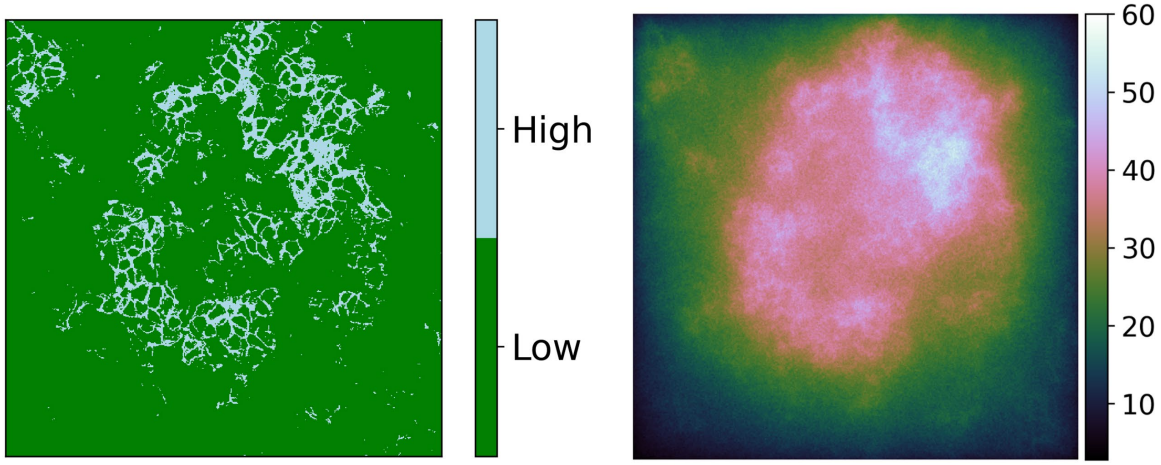

Tissue section B1 “low” $SSTR_2$ expression

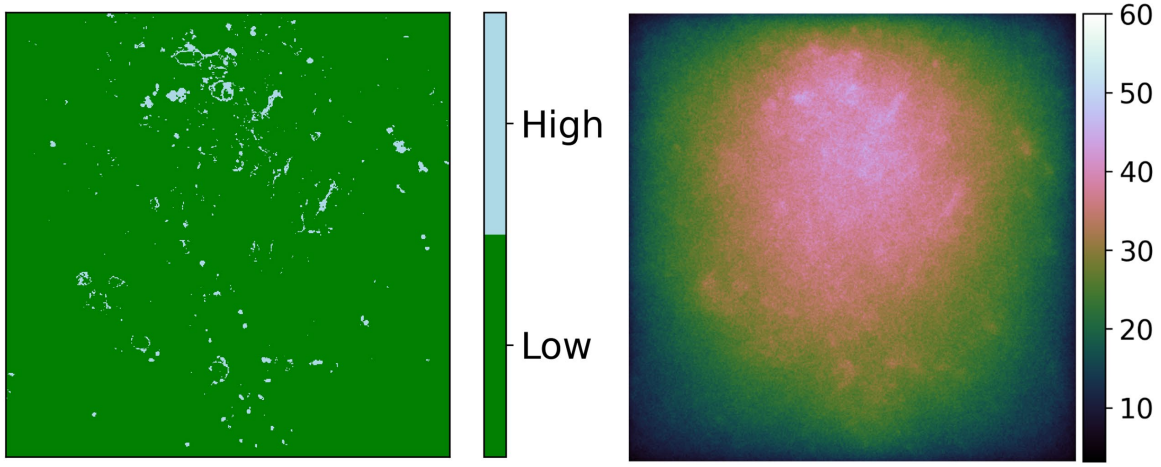

Tissue section B2 “high” $SSTR_2$ expression

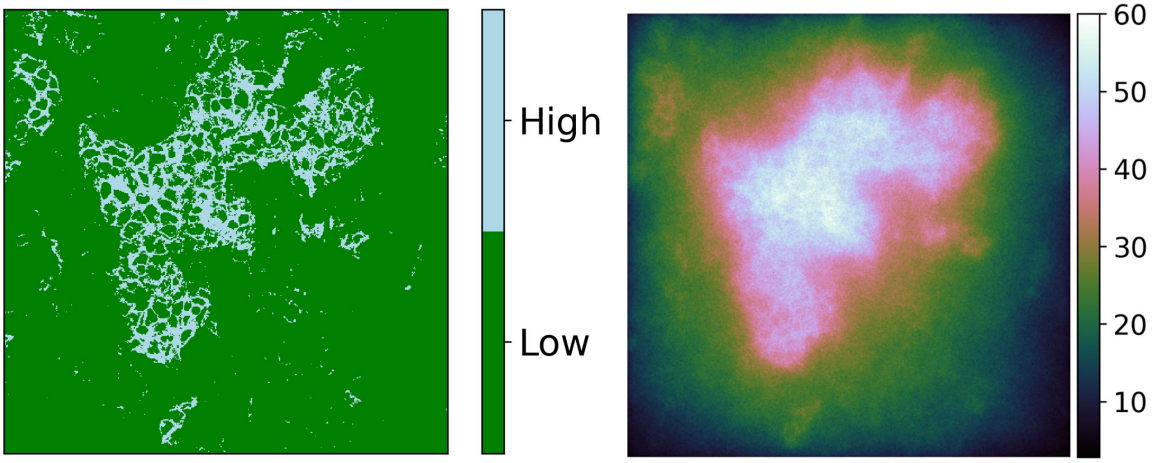

Tissue section B2 “low” $SSTR_2$ expression

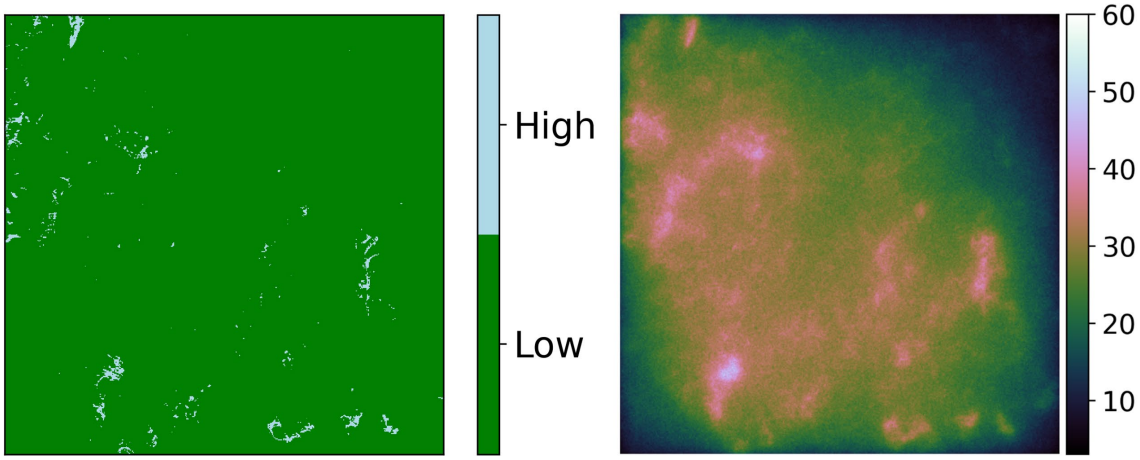

Tissue section B3 “high” $SSTR_2$ expression

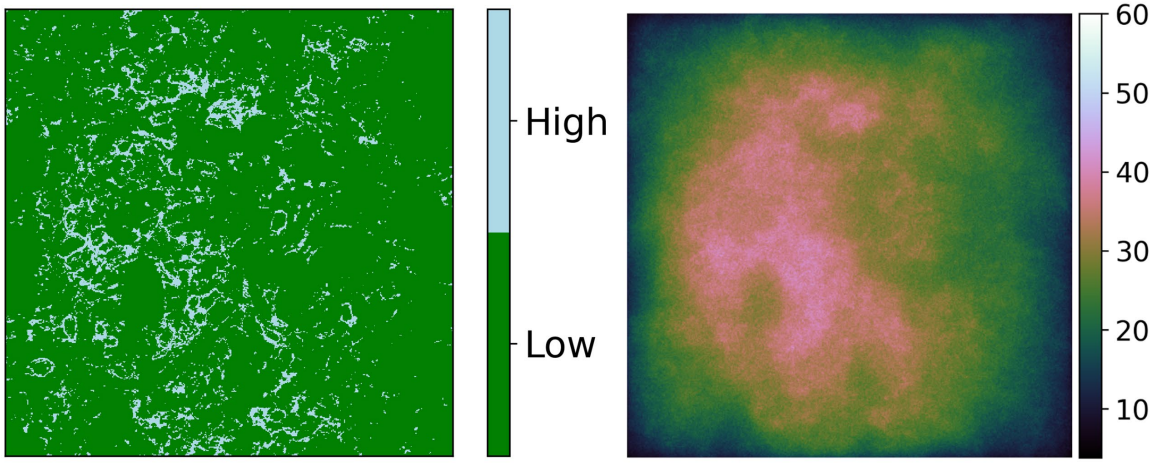

Tissue section B3 “low” $SSTR_2$ expression

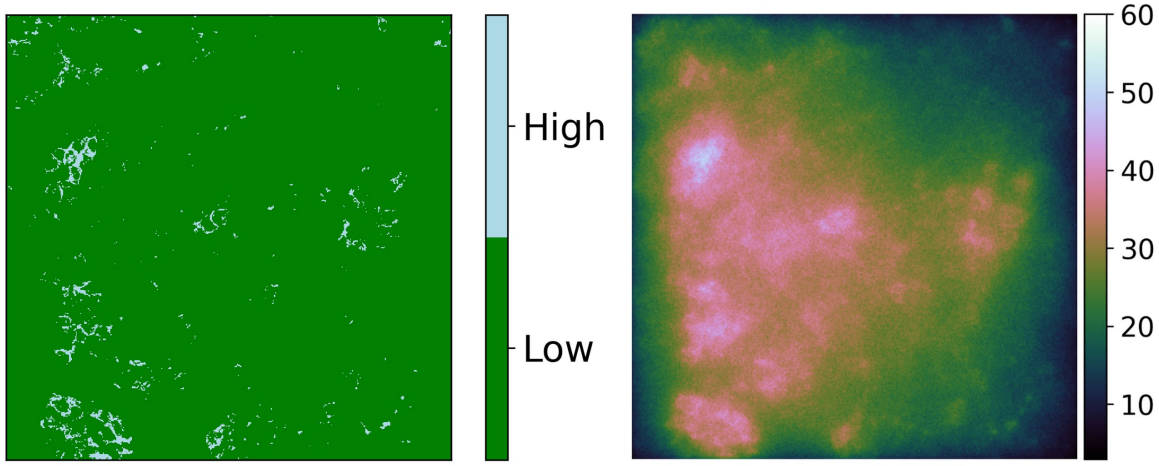

Tissue section B4 “high” SSTR2 expression

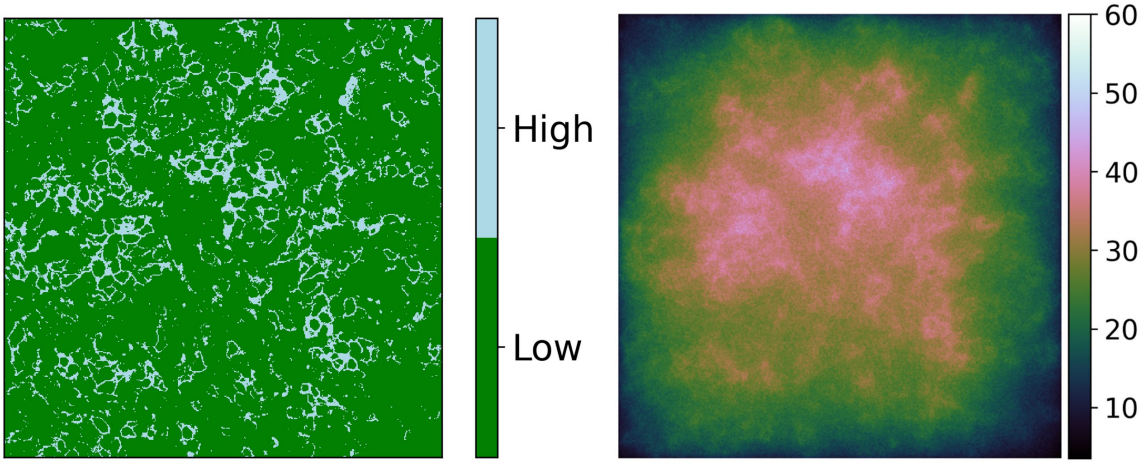

Tissue section B4 “low” SSTR2 expression

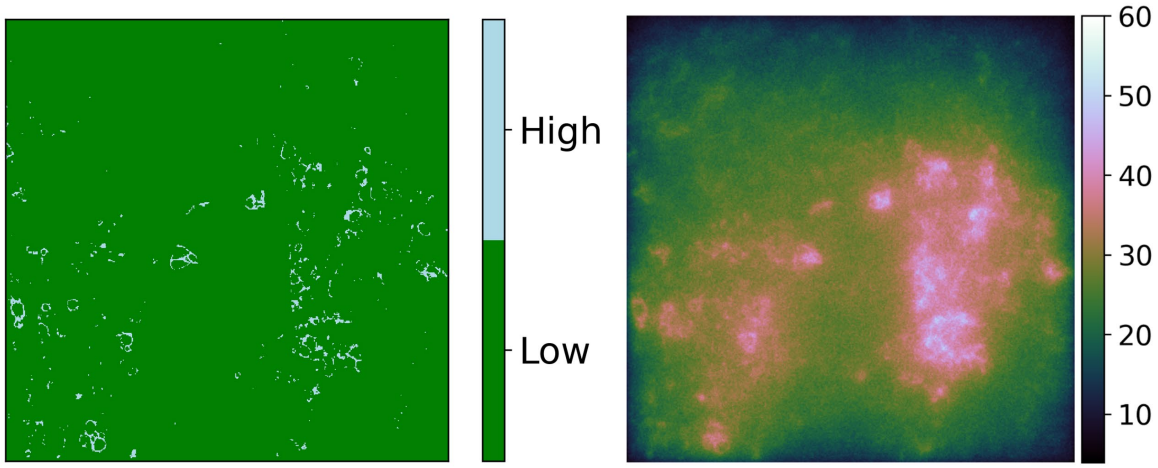

SUPPLEMENTAL FIGURE 3. Absorbed dose – DSBs correlation. Tile-scans (320 µm x 320 µm) of $SSTR_2$ staininings thresholded to identify low- (light blue) and high- (green) $SSTR_2$ expressing areas (on the left). Absorbed dose rate maps (at day 2) with color bar in Gy and mGy/h and DSBs stainings.

Tissue section B1 “high” $SSTR_2$ expression

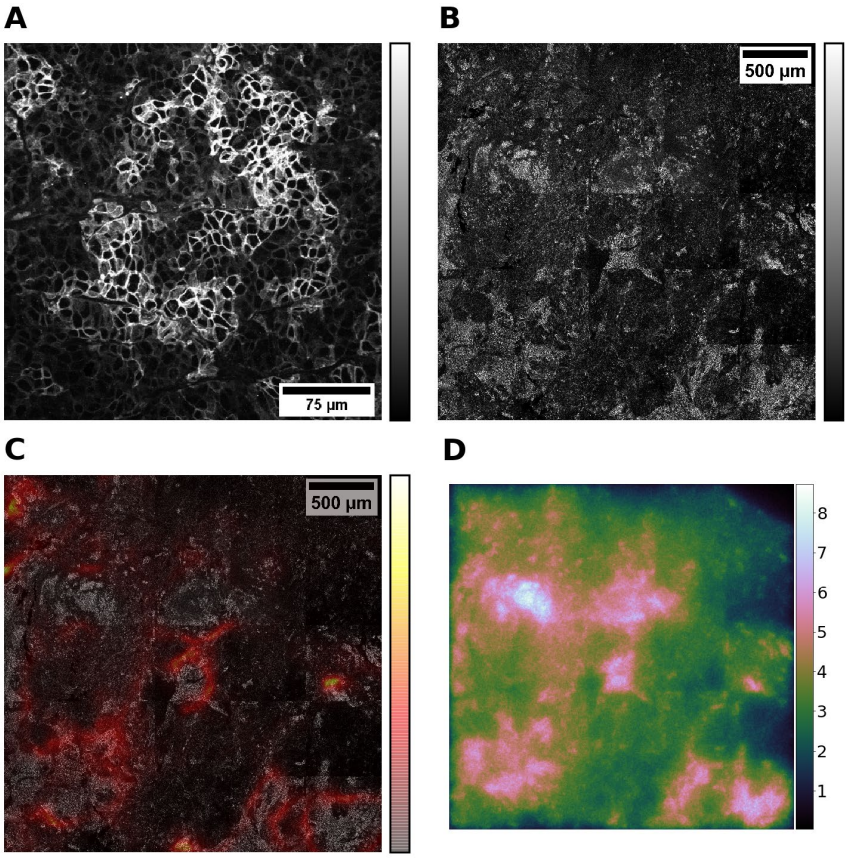

Tissue section B3 “high” $SSTR_2$ expression

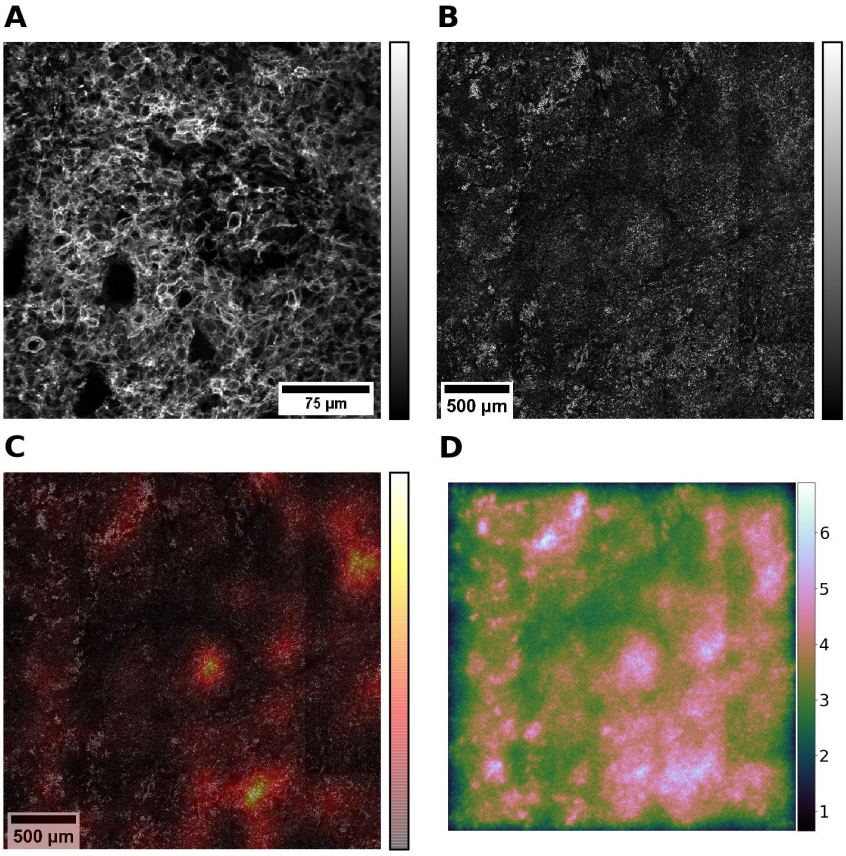

Tissue section B4 "high" $SSTR_2$ expression

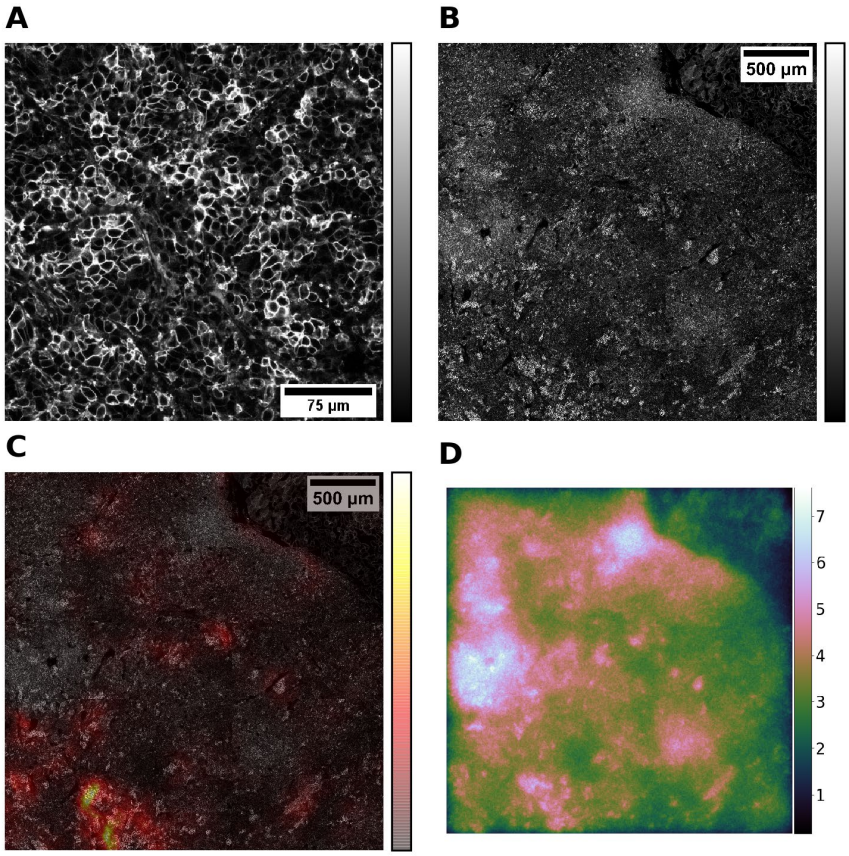

SUPPLEMENTAL FIGURE 4. Template matching technique. (A) Small tissue section used as template. (B) Large tissue section used as "test image". (C) Color map indicating the similarity score based on the χ^2 value overlaid on top of the large tissue section. Color bars indicate the pixel intensities of the tile-scans (greyscale) or similarity map (red-yellow). (D) Absorbed dose map with color bar in Gy.

Absorbed dose 0-2days and initial dose-rate
Tissue section A1

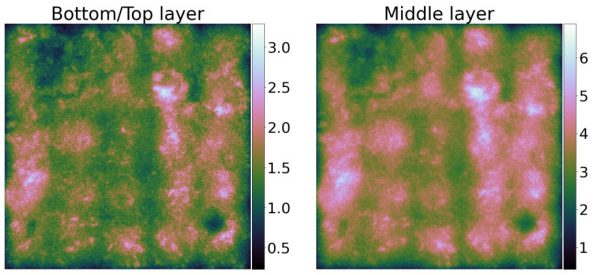

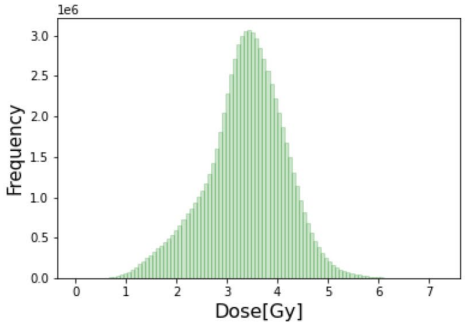

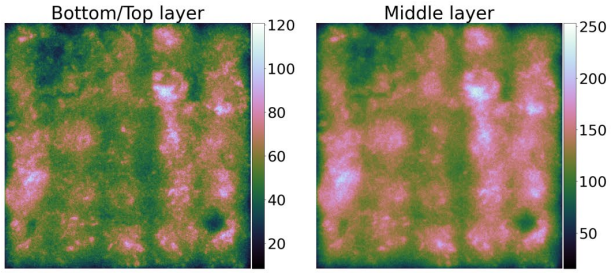

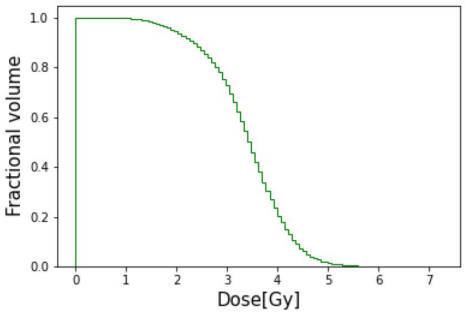

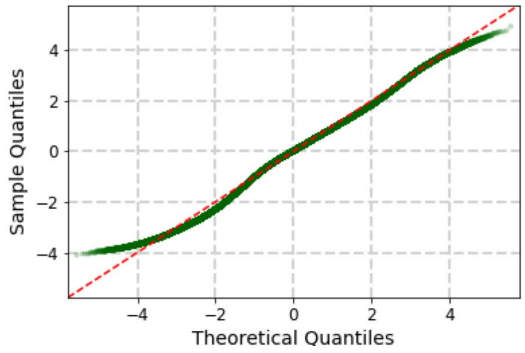

Tissue section A2

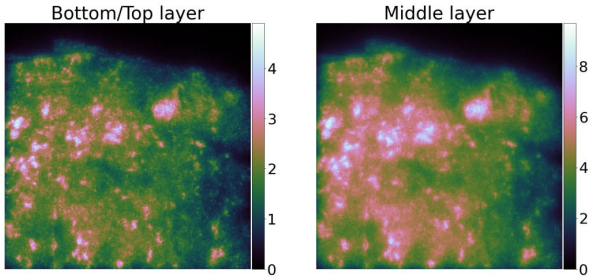

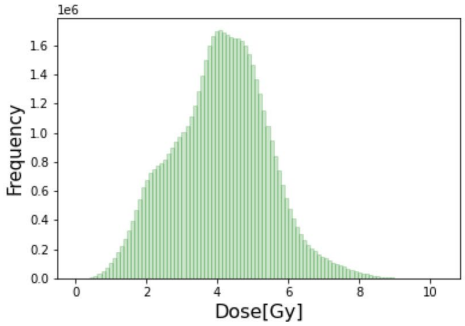

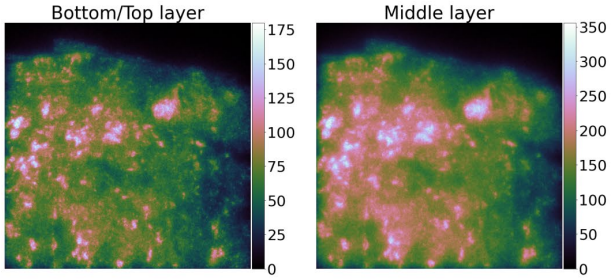

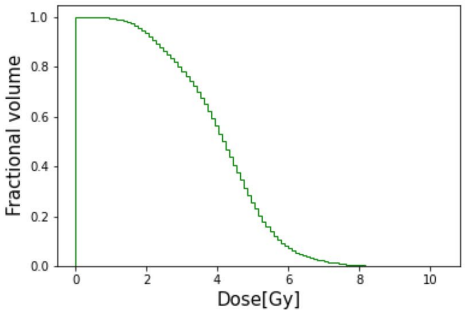

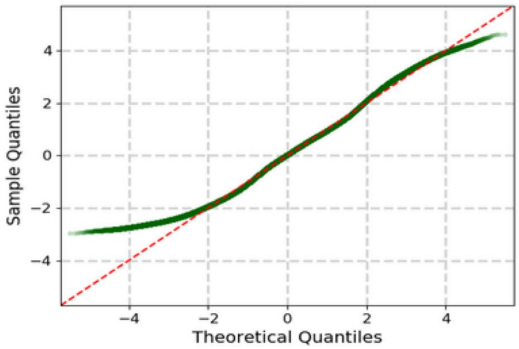

Tissue section A3

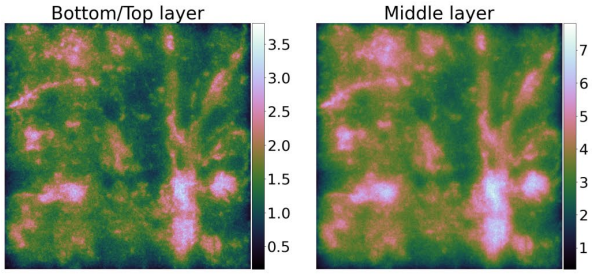

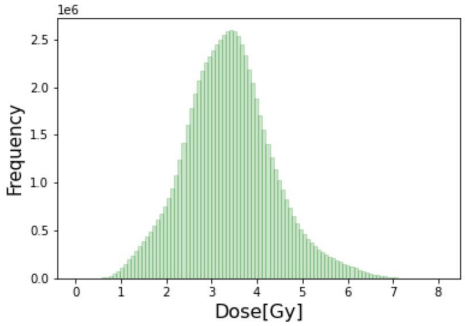

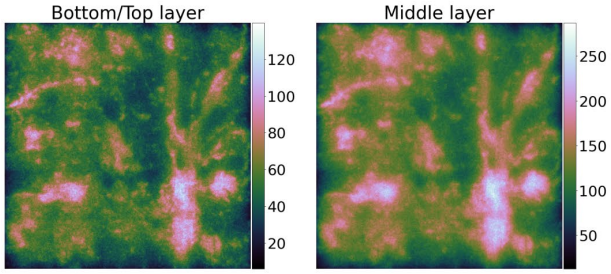

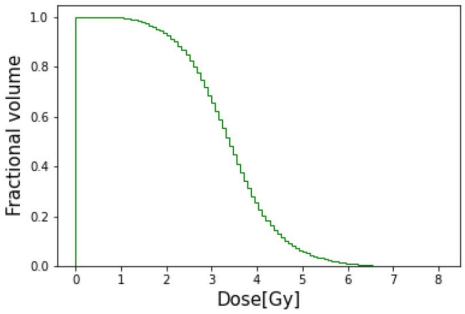

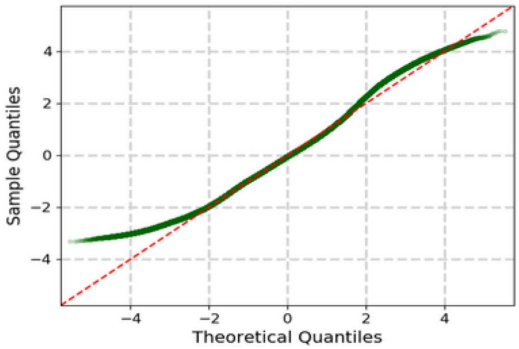

Tissue section A4

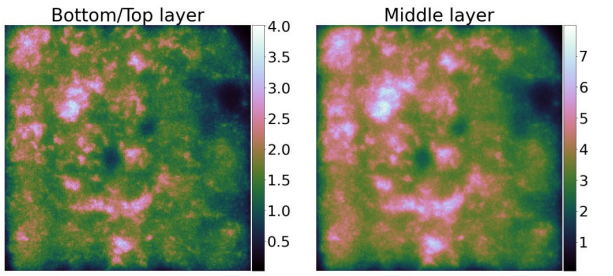

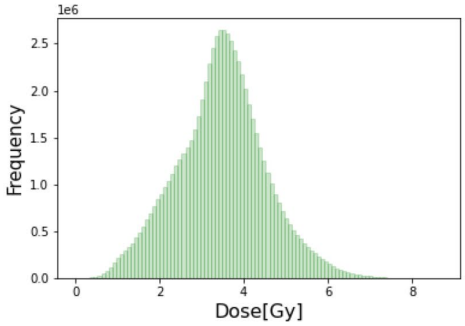

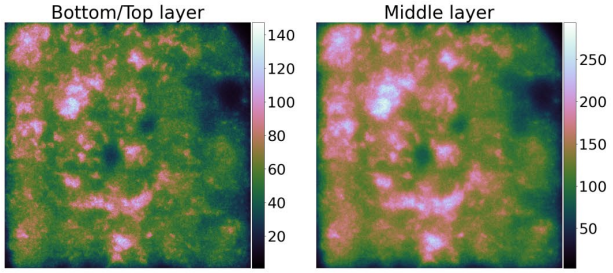

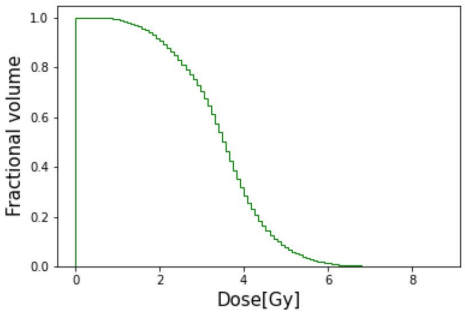

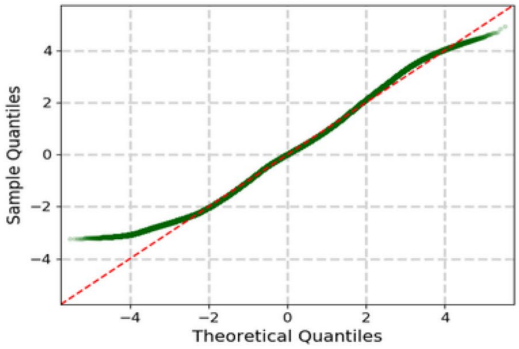

Equivalent uniform case

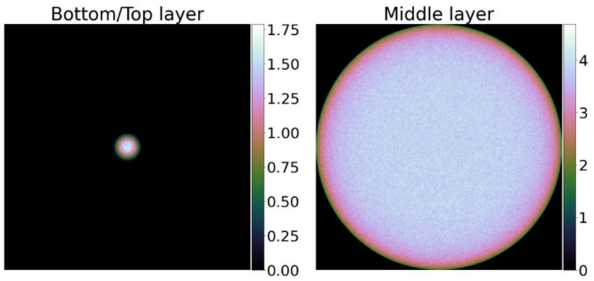

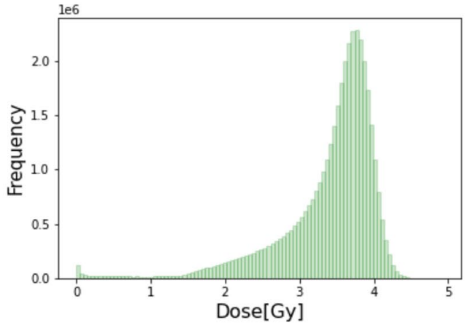

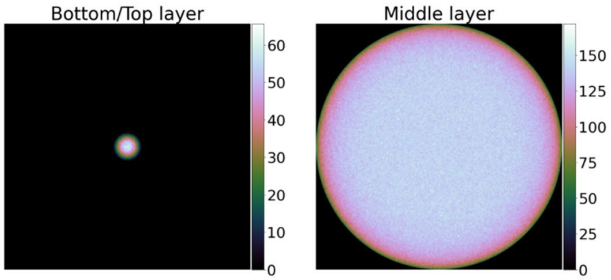

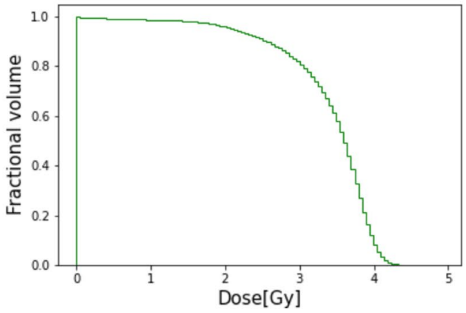

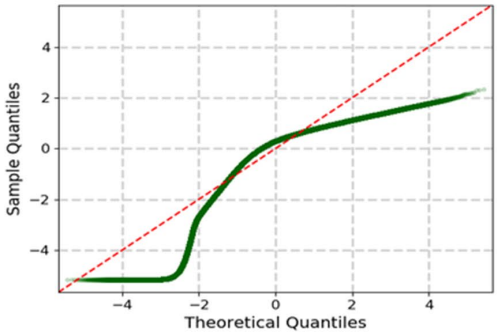

Absorbed dose 2-5 days and dose-rate at day 2

Tissue section B1

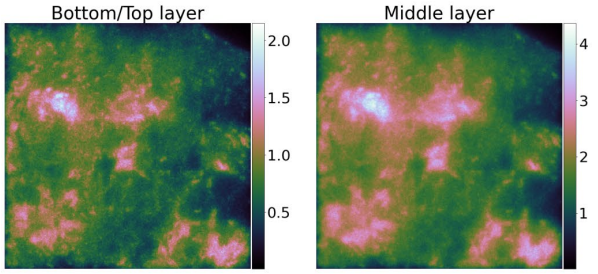

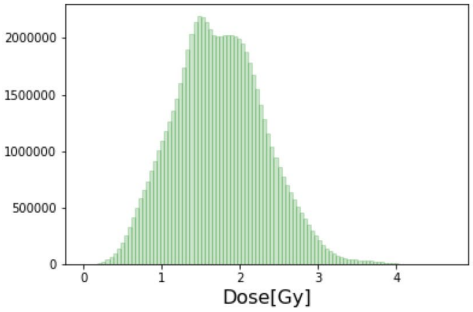

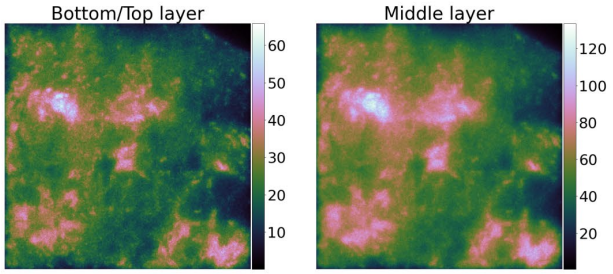

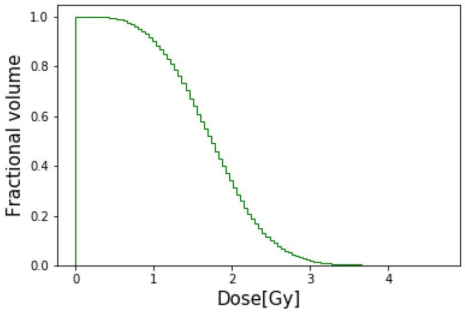

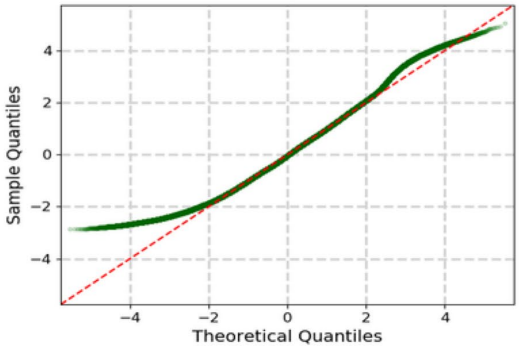

Tissue section B2

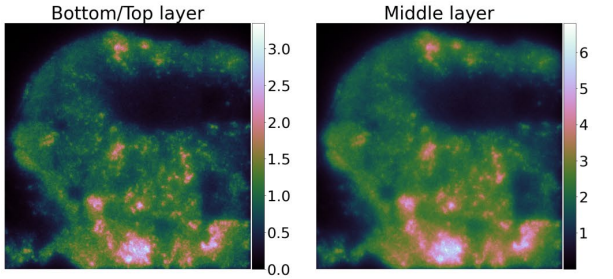

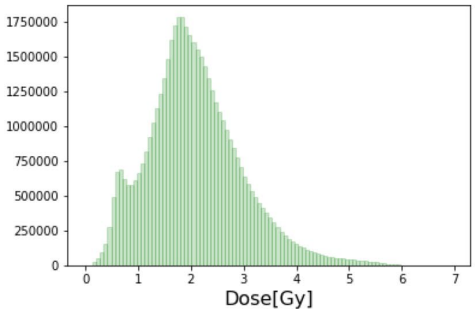

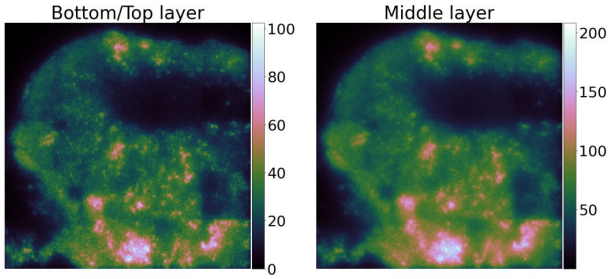

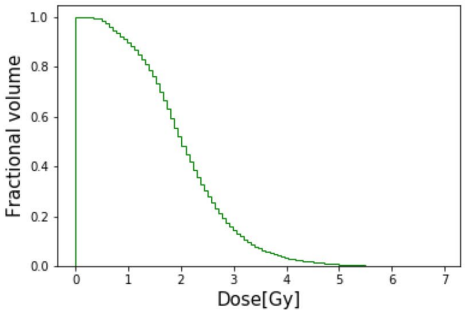

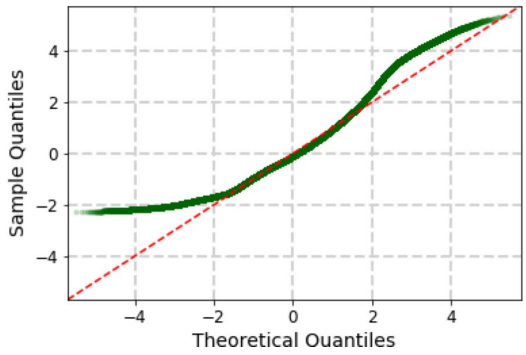

Tissue section B3

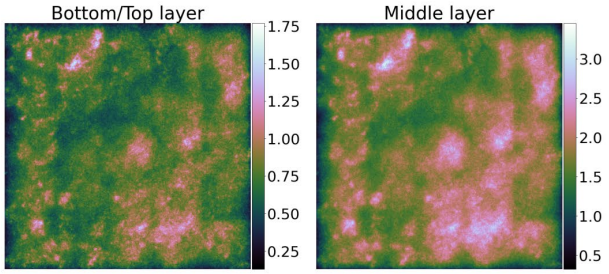

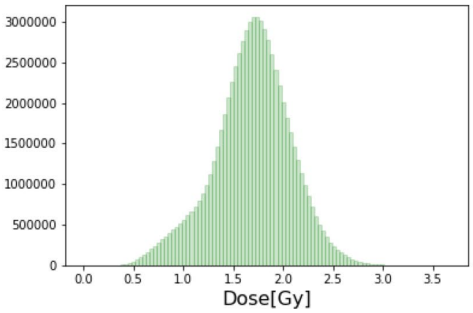

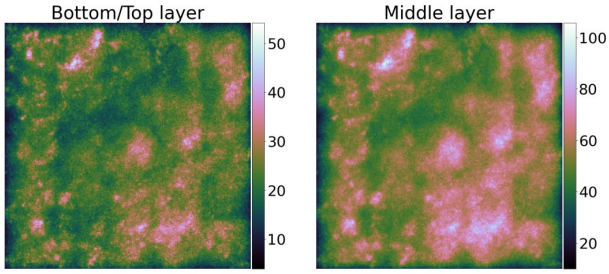

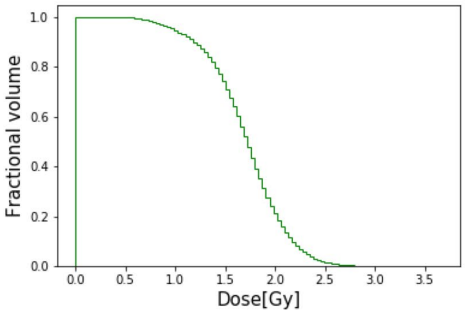

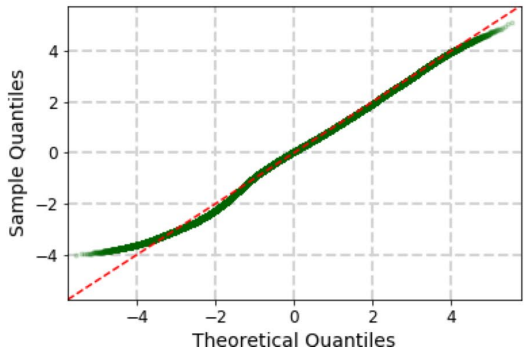

Tissue section B4

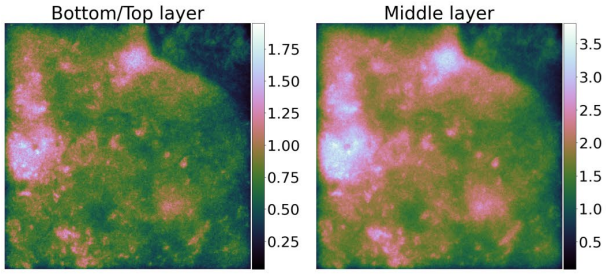

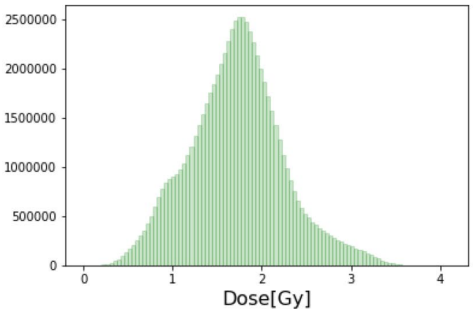

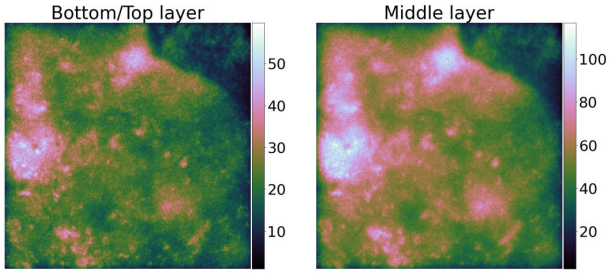

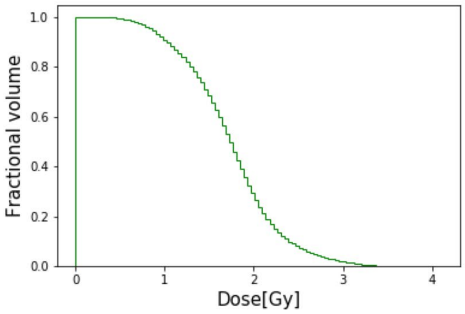

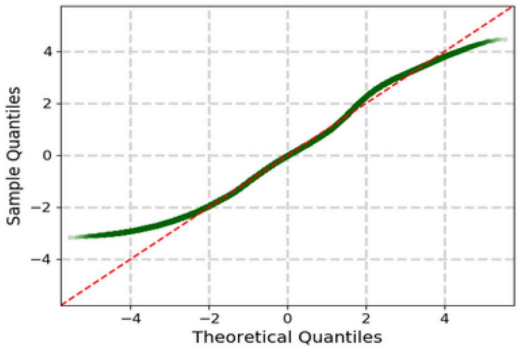

Equivalent uniform case

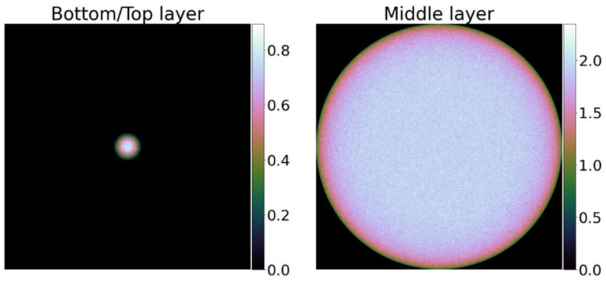

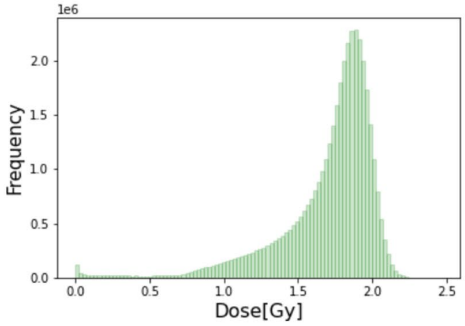

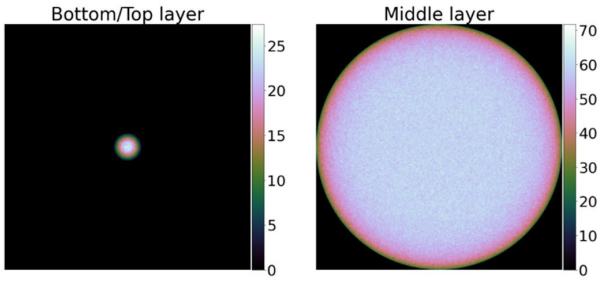

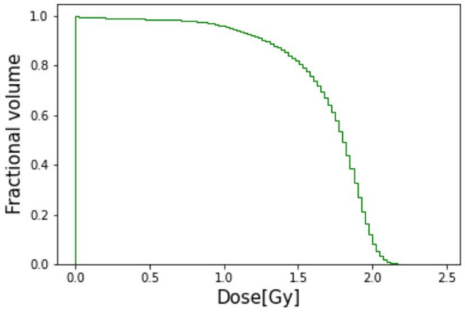

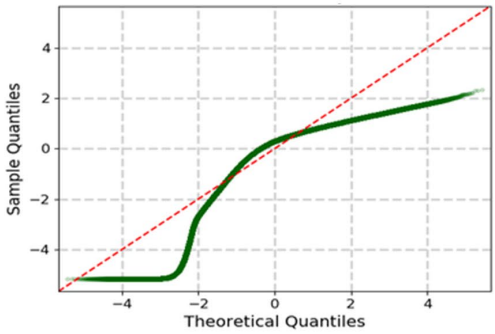

Absorbed dose 5-11 days and dose-rate at day 5
Tissue section C1

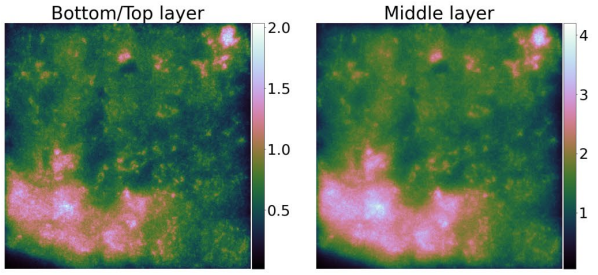

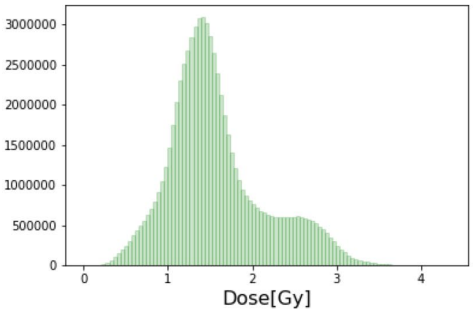

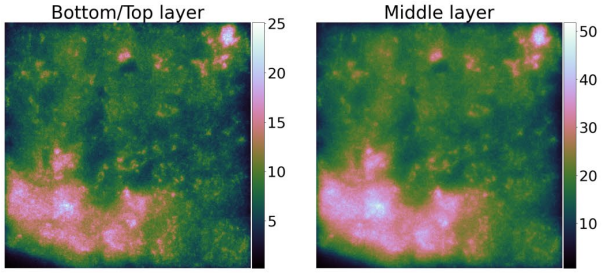

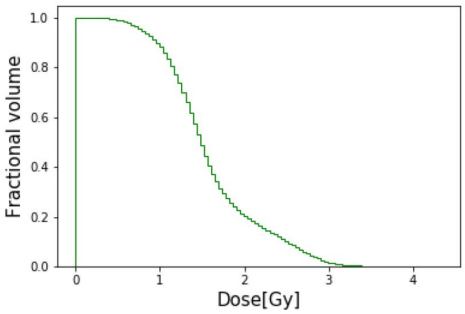

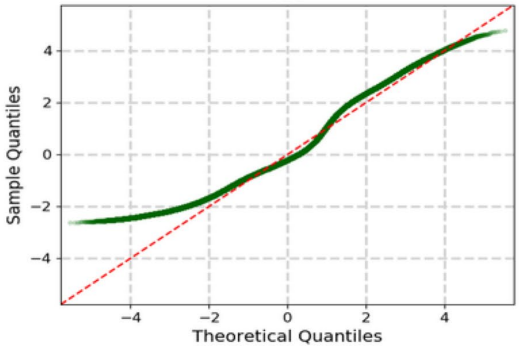

Tissue section C2

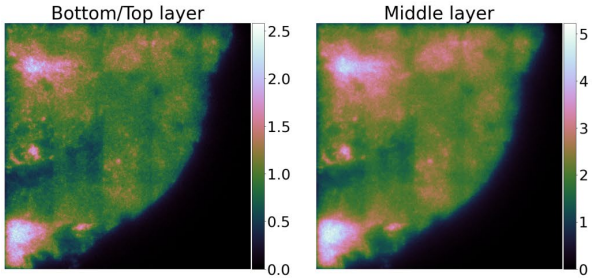

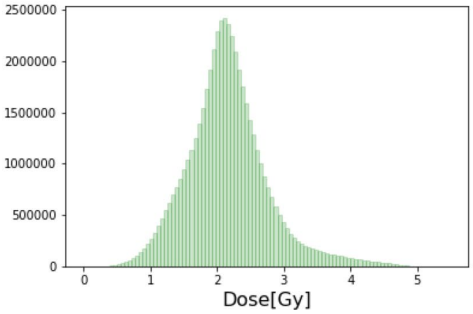

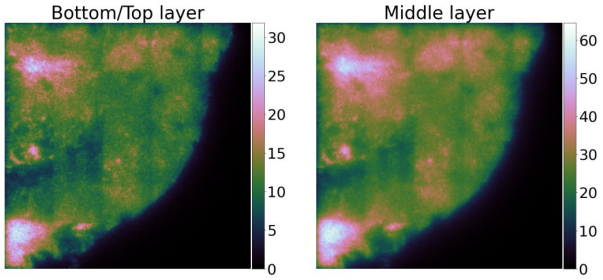

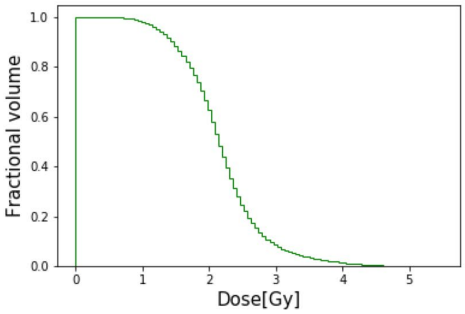

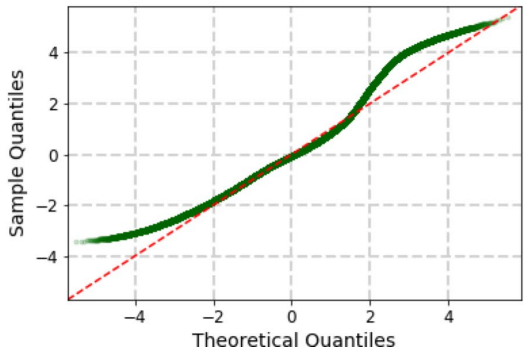

Tissue section C3

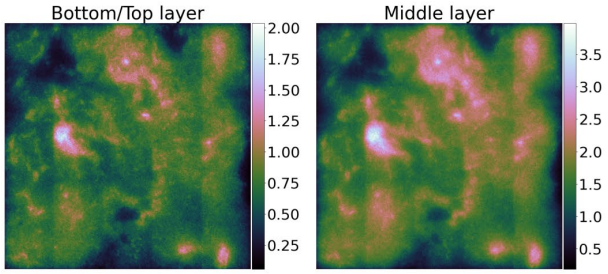

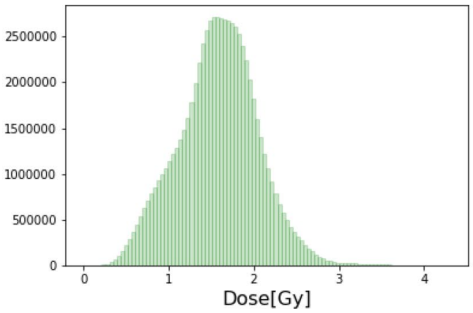

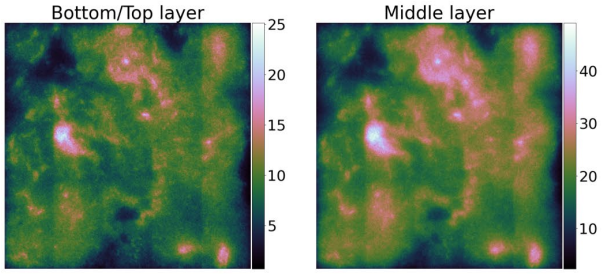

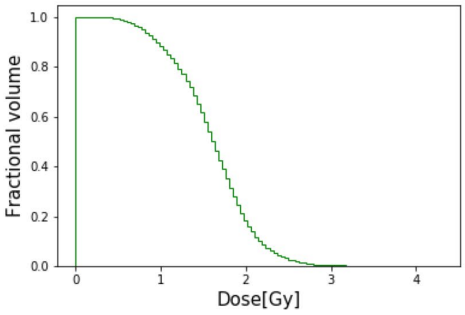

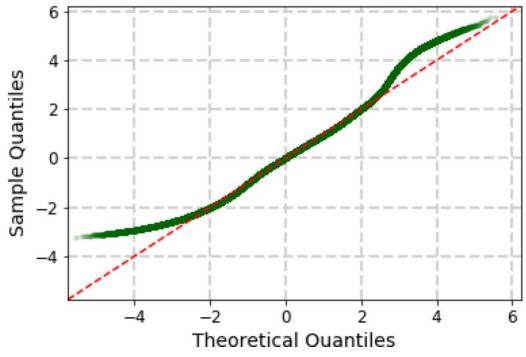

Tissue section C4

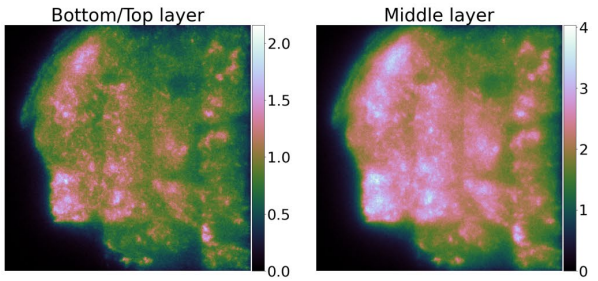

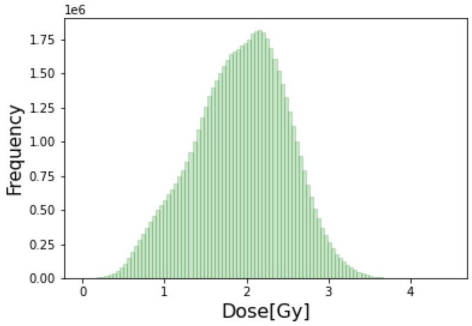

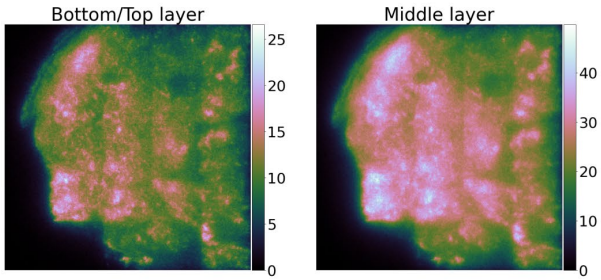

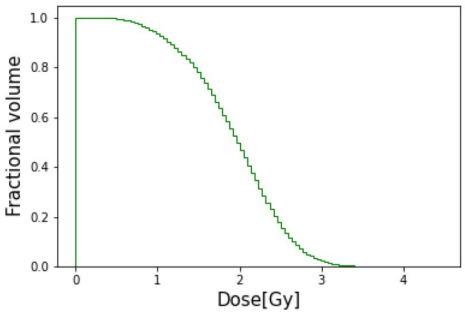

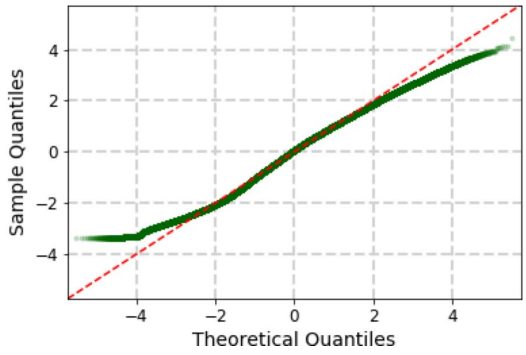

Equivalent uniform case

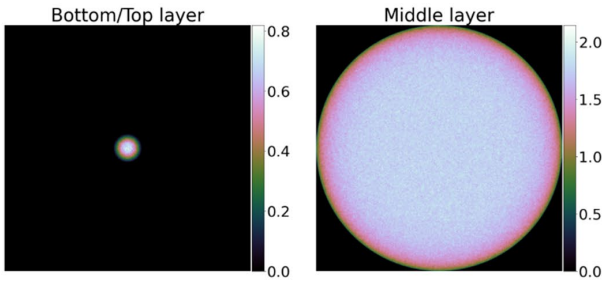

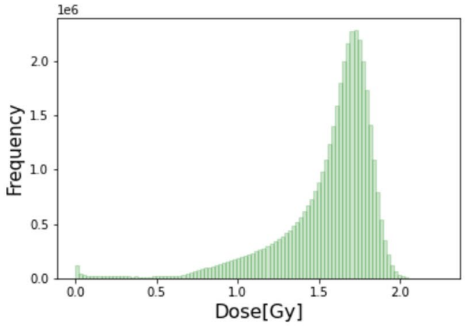

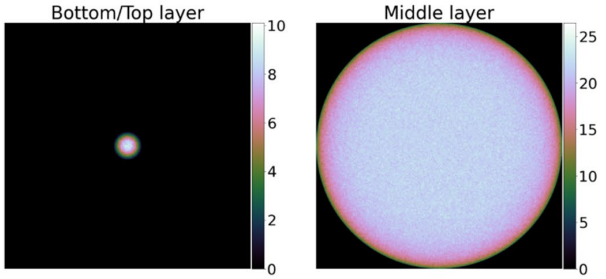

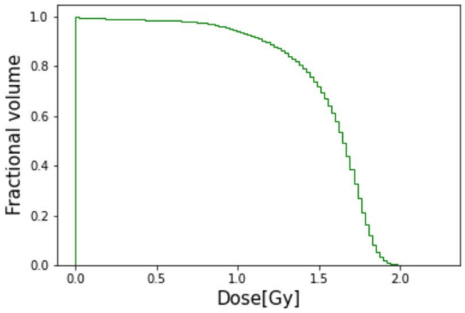

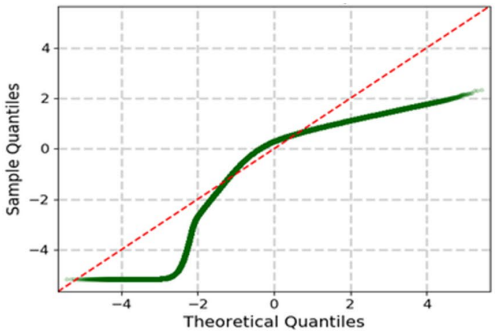

Absorbed dose 11-14 days and dose-rate at day 11

Tissue section D1

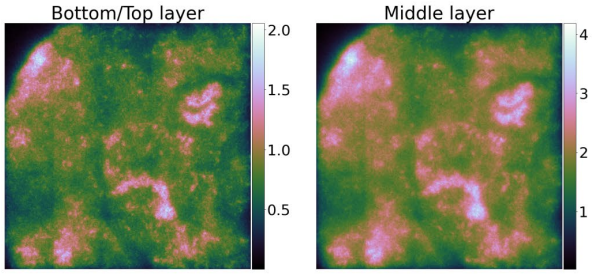

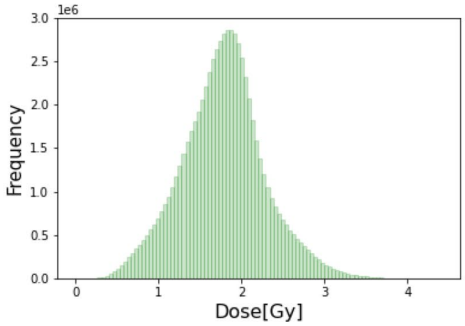

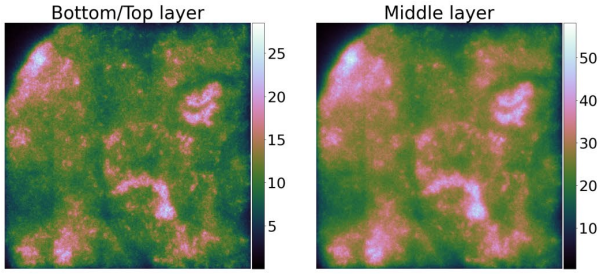

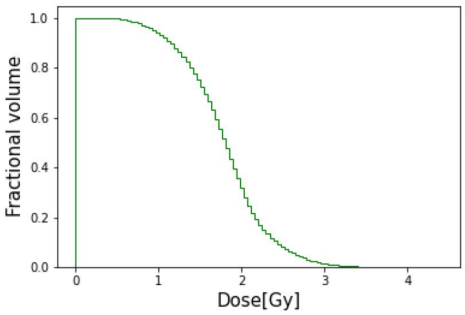

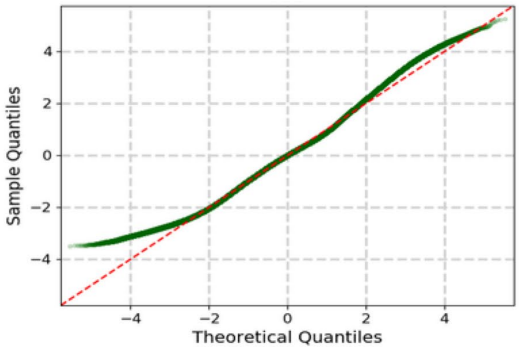

Tissue section D2

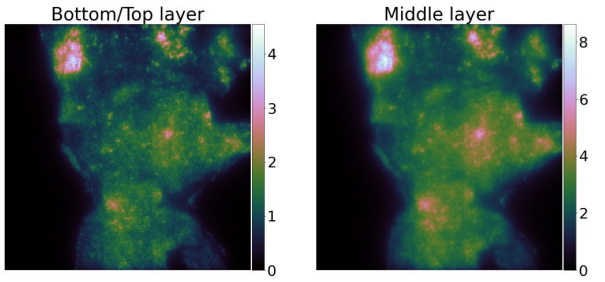

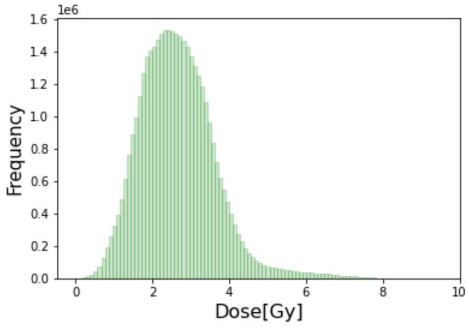

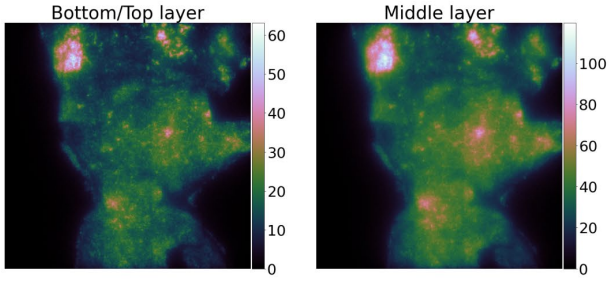

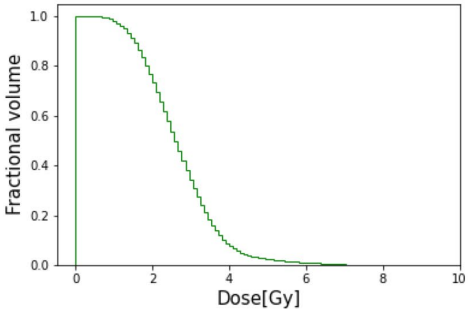

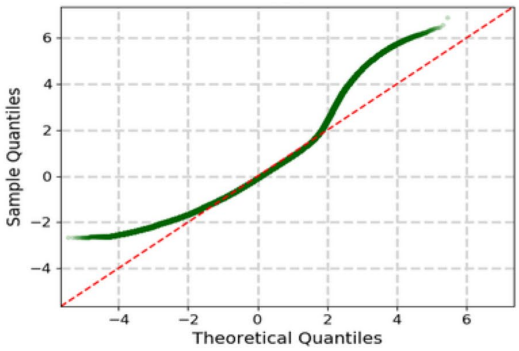

Tissue section D3

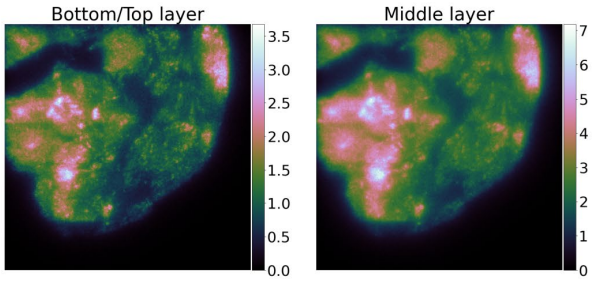

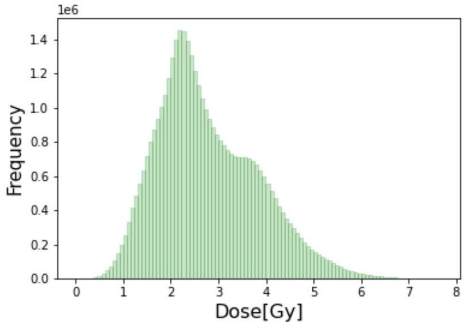

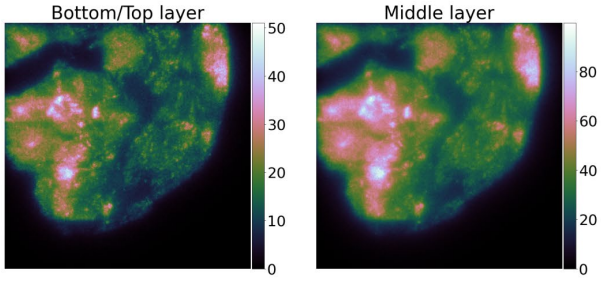

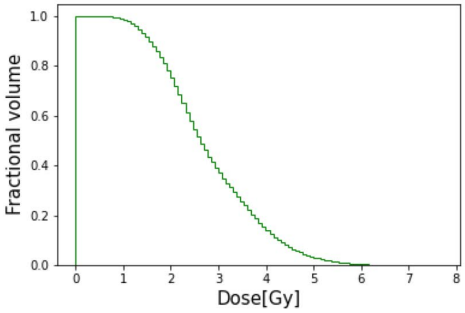

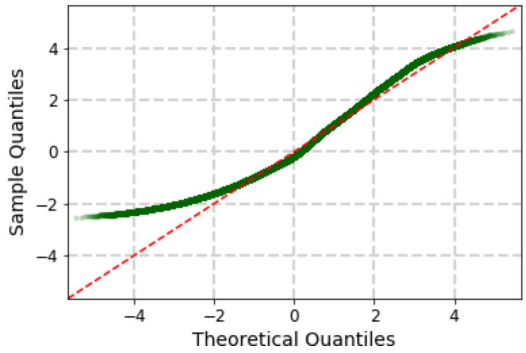

Tissue section D4

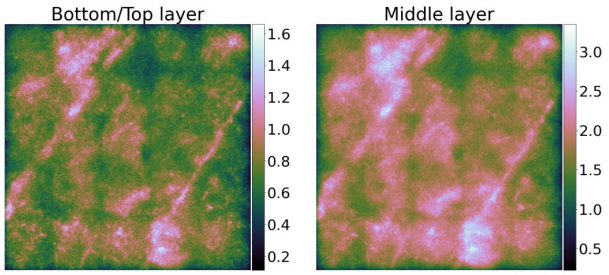

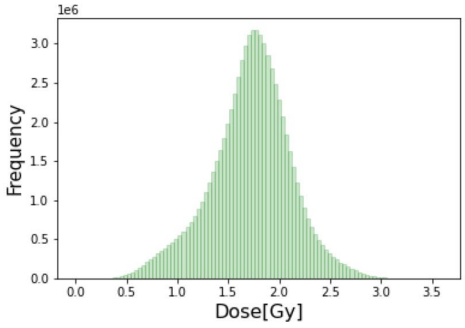

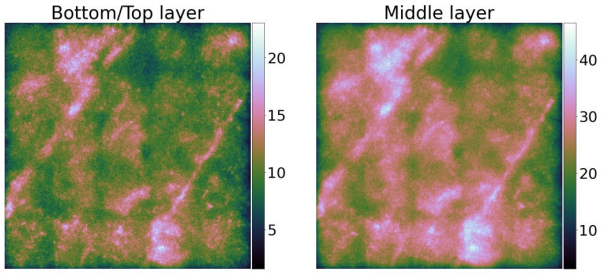

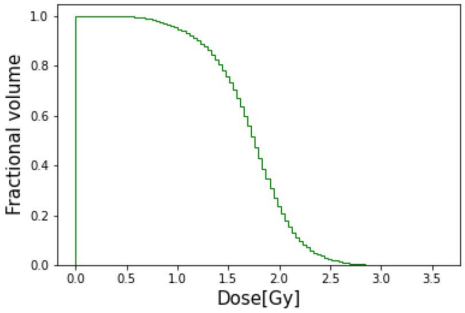

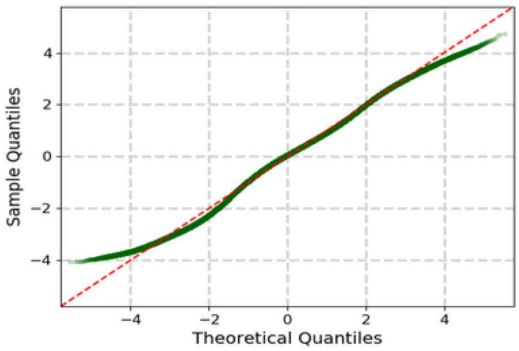

Equivalent uniform case

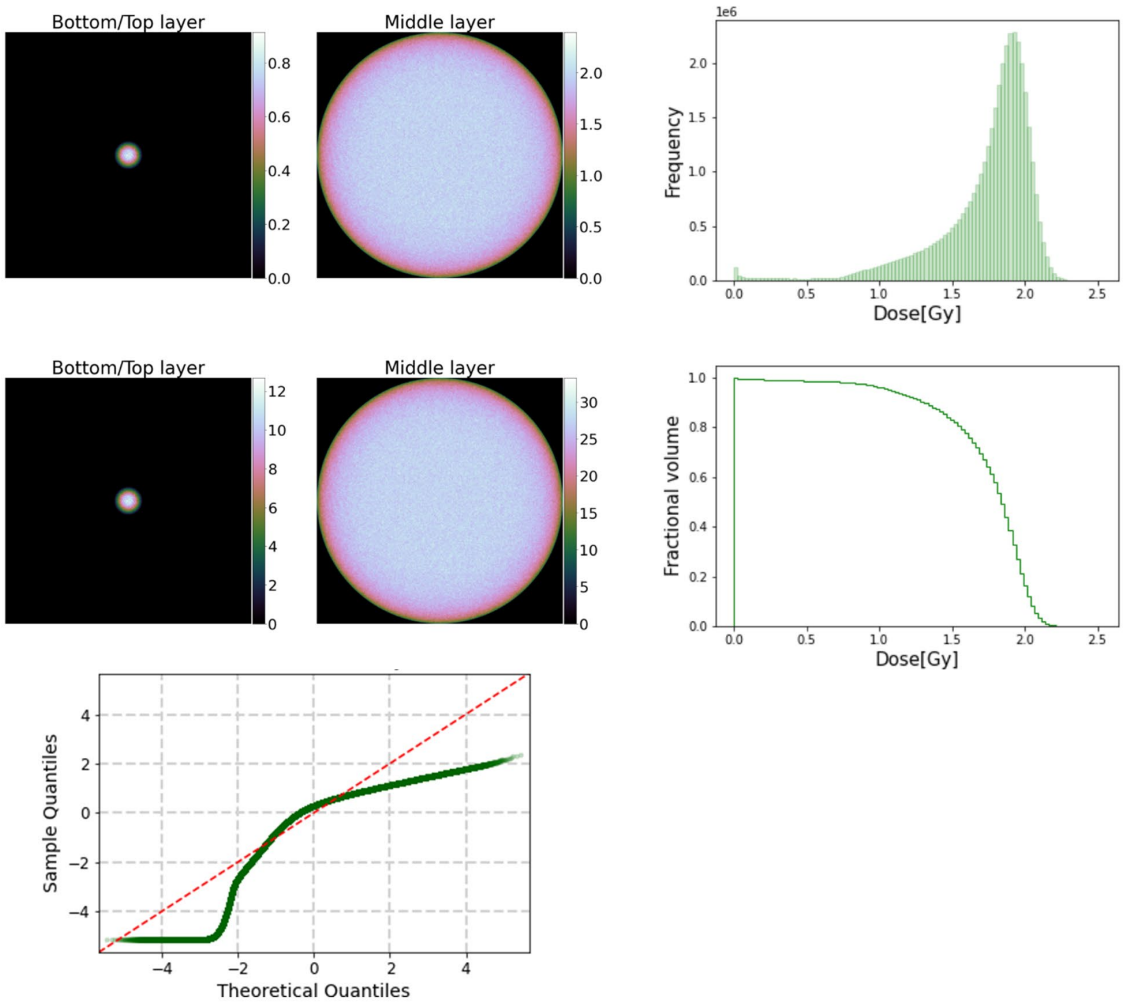

SUPPLEMENTAL FIGURE 5. Absorbed dose distributions corresponding to homogeneous and heterogeneous exposures reported by means of dose and dose rate maps (left side), frequency DVH and cumulative DVH (right side)and Q-Q plots (bottom). The generalized equivalent uniform dose (gEUD) for each tissue section is reported in Supplemental Table 2.

Parameters α=0.14 Gy^{-1}, α/β=5 Gy

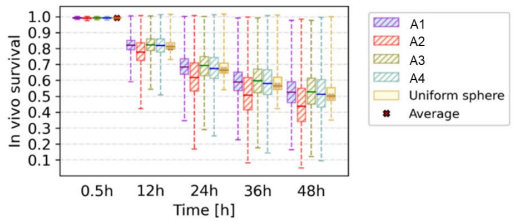

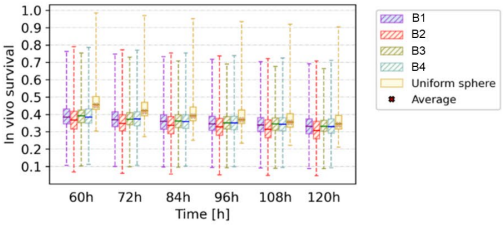

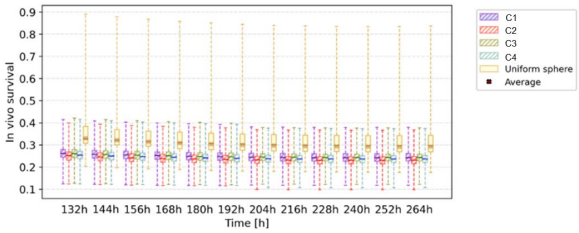

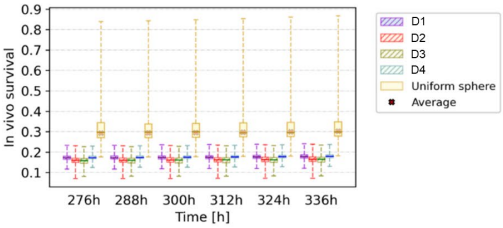

Parameters α=0.14 Gy^{-1}, α/β=10 Gy

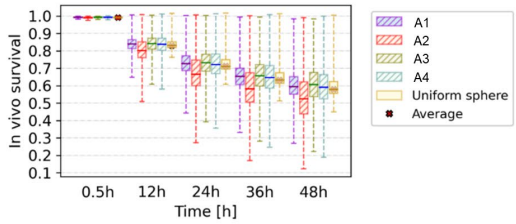

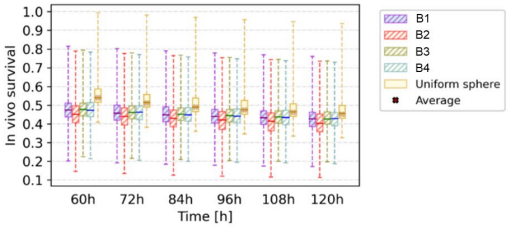

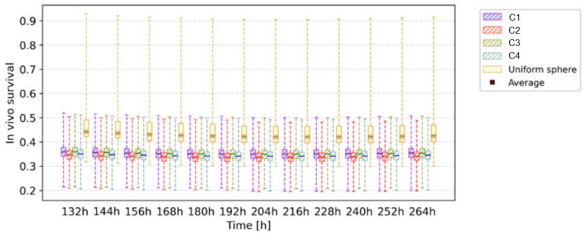

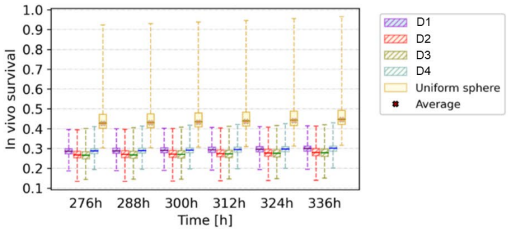

Parameters α=0.14 Gy^{-1}, α/β=100 Gy

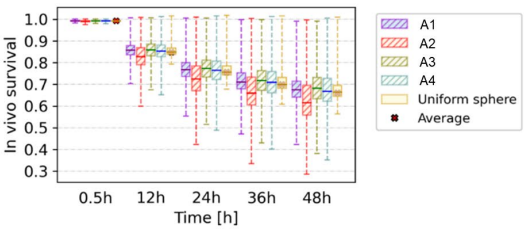

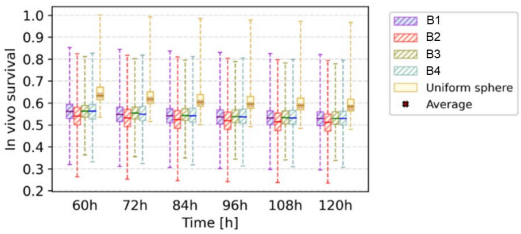

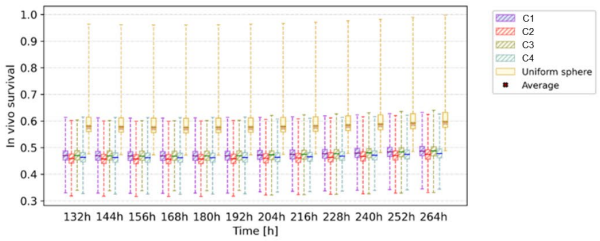

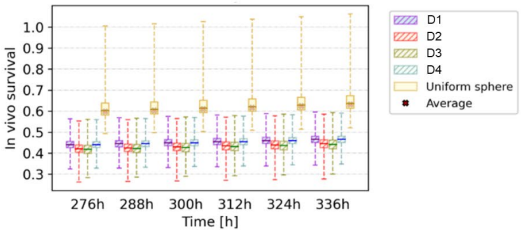

Parameters α=0.264 Gy^{-1}, α/β=5 Gy

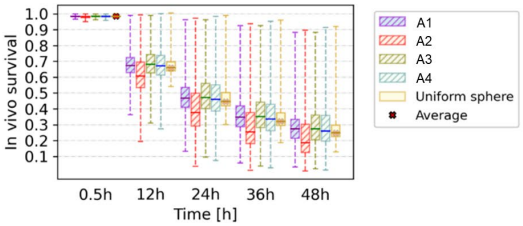

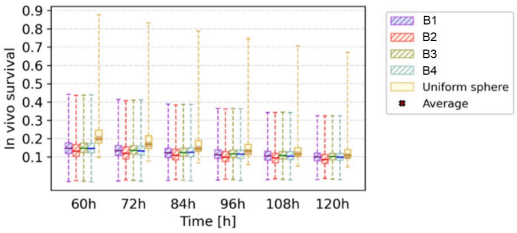

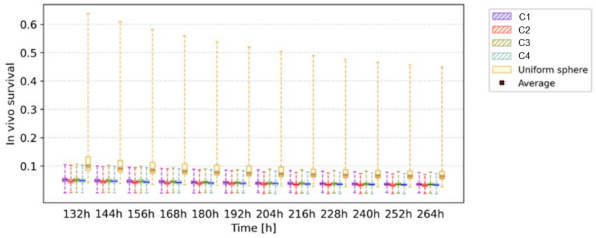

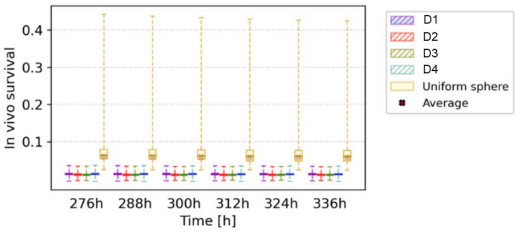

Parameters α=0.264 Gy^{-1}, α/β=10 Gy

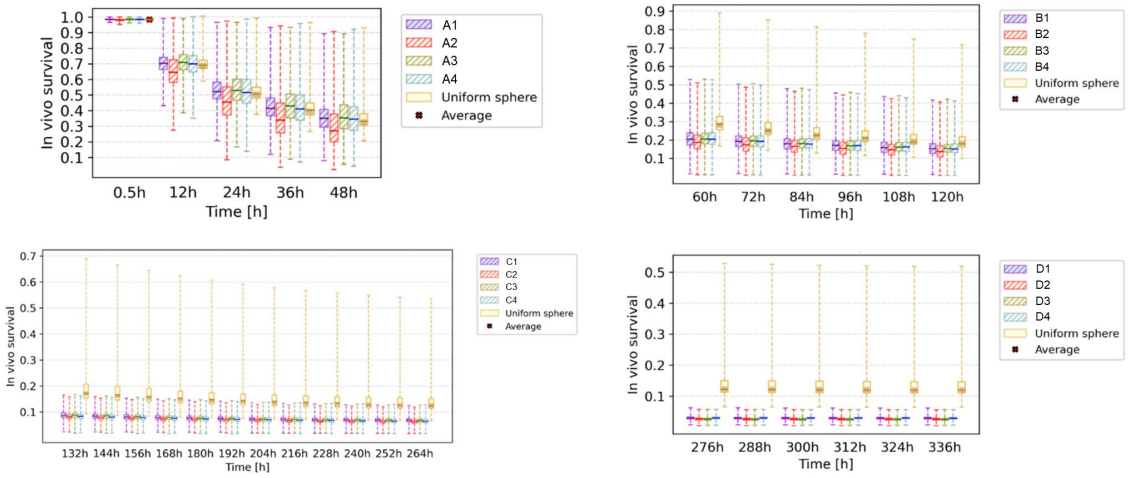

Parameters α=0.264 Gy^{-1}, α/β=100 Gy

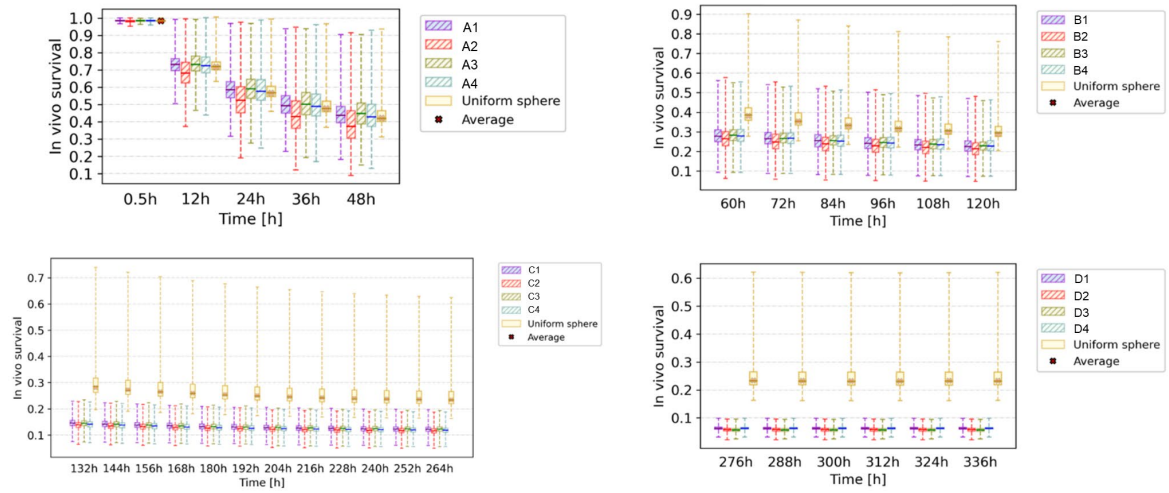

SUPPLEMENTAL FIGURE 6. Box plots indicating the *in vivo* survival distribution over time for constant values of α and β on different excised tissue sections. The whiskers correspond to 1.5 times the interquartile range.

Parameters α=(0.14±0.03) Gy^{-1}, α/β=5 Gy

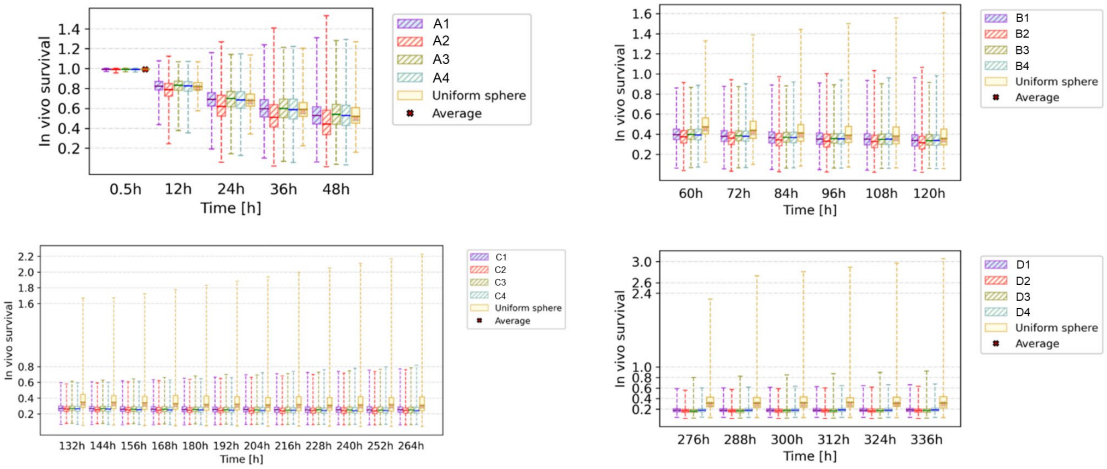

Parameters α=(0.14±0.03) Gy^{-1}, α/β=10 Gy

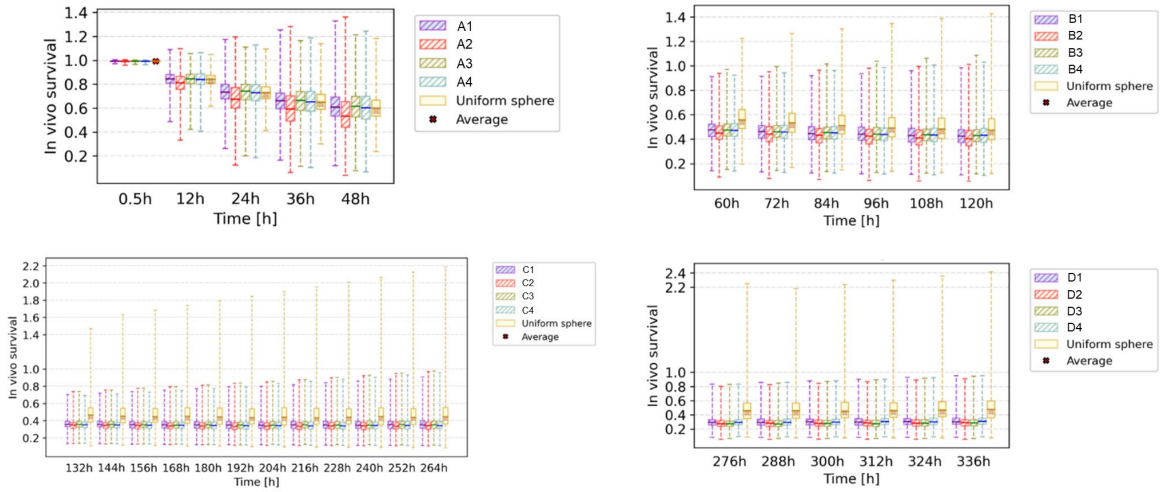

Parameters α=(0.14±0.03) Gy^{-1}, α/β=100 Gy

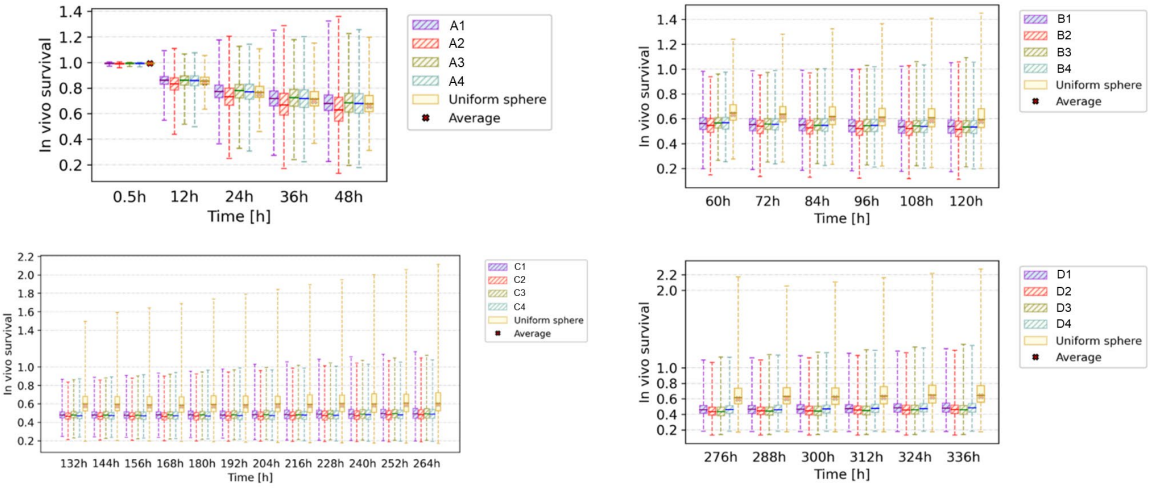

Parameters α=(0.264±0.04) Gy^{-1}, α/β=5 Gy

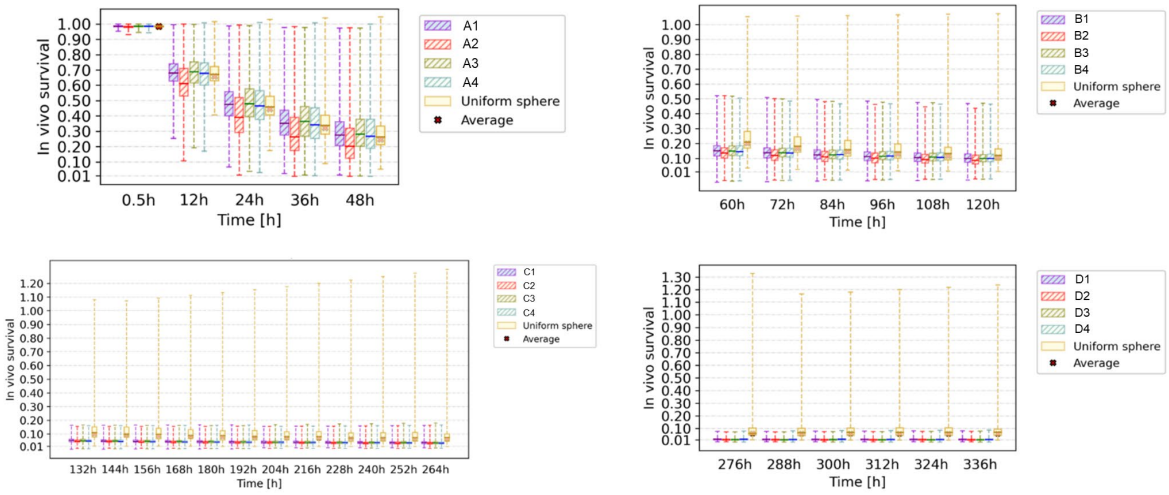

Parameters α=(0.264±0.04) Gy^{-1}, α/β=10 Gy

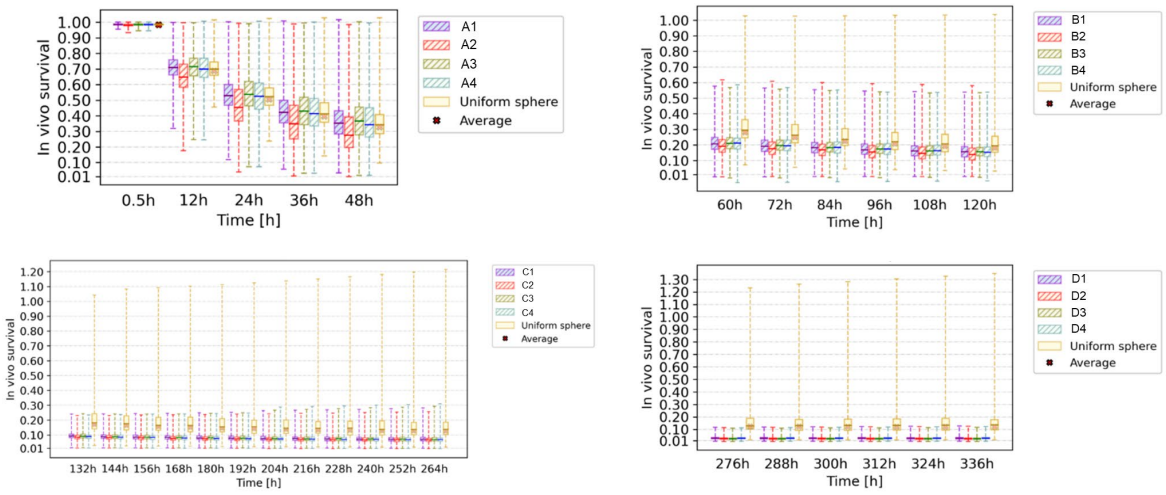

Parameters α=(0.264±0.04) Gy^{-1}, α/β=100 Gy

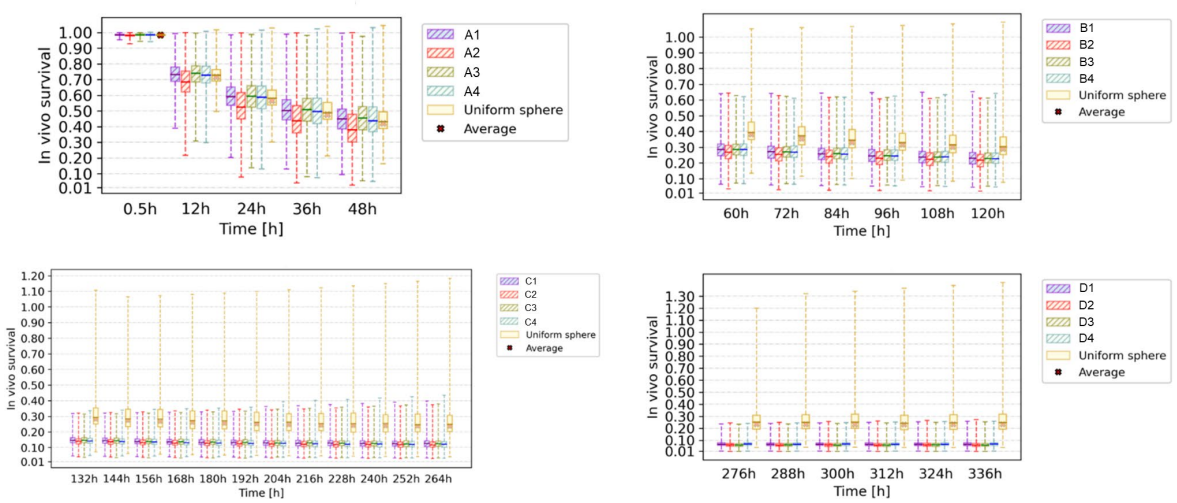

SUPPLEMENTAL FIGURE 7. Box plots indicating the *in vivo* survival distribution over time for Gaussian distributed α and β values on different excised tissue sections. The whiskers correspond to 1.5 times the interquartile range.

Heterogeneous dose distribution - Gaussian sensitivity

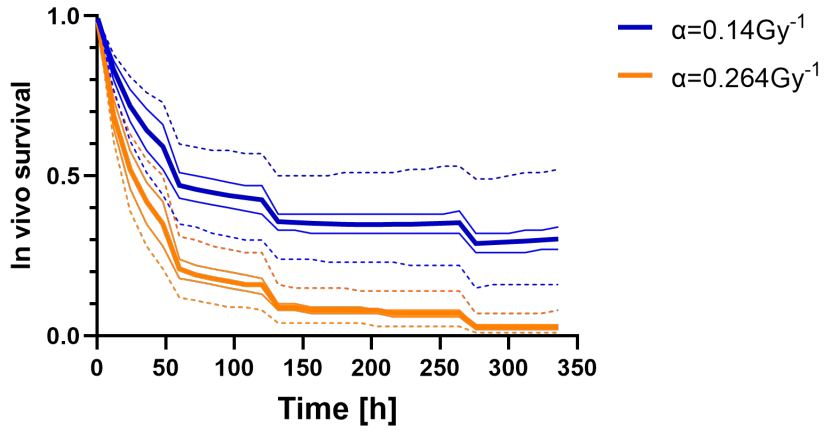

Uniform dose distribution - constant sensitivity

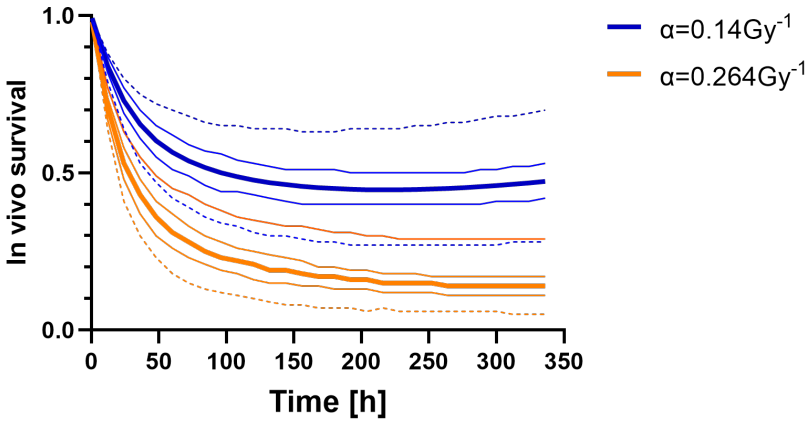

Uniform dose distribution - Gaussian sensitivity

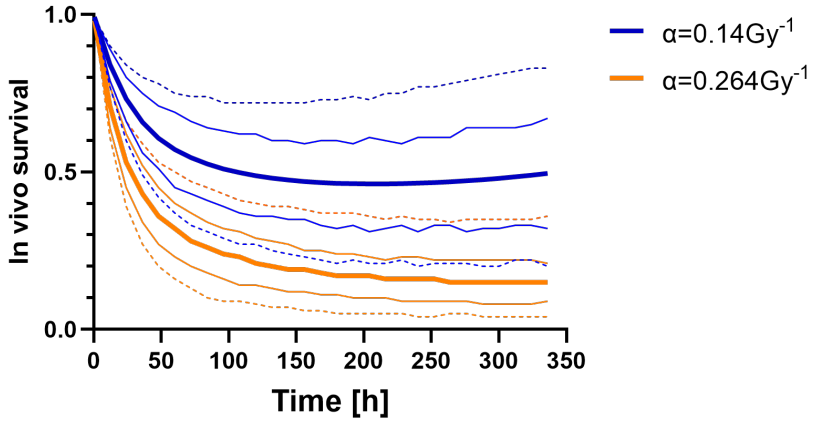

SUPPLEMENTAL FIGURE 8. Radiosensitivity parameter analysis for the modelled *in vivo* survival obtained using heterogeneous or uniform radionuclide distribution. The sensitivity parameters are either constant or Gaussian distributed. For each α value, the upper and lower dashed lines indicate the upper and

lower 1 SD limit corresponding to α/β=100 Gy and α/β=5 Gy, respectively. The continuous lines correspond to α/β=10.

Δt (days)	Tumor volume nomenclature	Volume (mm^3) (tumor cells %)	S-value (Gy/decay)	Average absorbed dose (Gy) (range)	Heterogeneity*	Average dose in each Δt (Gy)	Dose for homogenous exposure (range) (Gy)
0-2	A1	23.75 (99.70%)	8.78E-10 ± 3.38E-12	3.37 ± 0.01 (0.16 - 7.25)	54.45%	3.57 ± 0.34	3.43± 0.09 (0.00 – 4.92)
	A2	17.44 (96.16%)	1.07E-09 ± 3.40E-12	4.09 ± 0.01 (0.10 - 10.32)	53.19%		
	A3	23.57 (99.40%)	8.82E-10 ± 3.37E-12	3.38 ± 0.01 (0.16 - 8.07)	48.34%		
	A4	22.26 (98.51%)	9.03E-10 ± 3.36E-12	3.46 ± 0.01 (0.03 - 8.70)	50.07%		
2-5	B1	22.39 (98.50%)	9.04E-10 ± 3.39E-12	1.74 ± 0.01 (0.07 – 4.68)	49.02%	1.80 ± 0.18	1.72± 0.05 (0.00 – 2.47)
	B2	15.45 (94.18%)	1.08E-09 ± 3.42E-12	2.08 ± 0.01 (0.03 – 6.94)	45.14%		
	B3	23.27 (98.86%)	8.78E-10 ± 3.38E-12	1.69 ± 0.01 (0.13 – 3.67)	51.94%		
	B4	22.80 (99.06%)	8.95E-10 ± 3.39E-12	1.72 ± 0.01 (0.05 – 4.11)	49.61%		
5-11	C1	22.71 (98.08%)	8.97E-10 ± 3.38E-12	1.57 ± 0.01 (0.07 – 4.34)	40.73%	1.81 ± 0.29	1.57±0.04 (0.00 – 2.25)
	C2	16.39 (99.17%)	1.23E-09 ± 3.43E-12	2.16 ± 0.01 (0.05 – 5.48)	48.51%		
	C3	23.09 (99.31%)	9.01E-10 ± 3.38E-12	1.58 ± 0.01 (0.05 – 4.30)	50.23%		
	C4	19.13 (98.97%)	1.10E-09 ± 3.36E-12	1.92 ± 0.01 (0 – 4.46)	52.52%		
11-14	D1	22.73 (98.76%)	9.07E-10 ± 3.37E-12	1.78 ± 0.01 (0.02 – 4.41)	51.78%	2.23 ± 0.56	1.75±0.05 (0.00 -2.52)
	D2	12.51 (93.69%)	1.35E-09 ± 3.42E-12	2.65 ± 0.01 (0.01 – 9.53)	45.91%		
	D3	12.99 (96.28%)	1.42E-09 ± 3.43E-12	2.77 ± 0.01 (0.12 – 7.69)	43.67%		
	D4	23.93 (99.67%)	8.75E-10 ± 3.39E-12	1.71 ± 0.01 (0.11 – 3.59)	51.66%		
Average			1.01E-09 ± 3.39E-12		49.17% ± 3.72%		
Cumulative (0-14 days)						8.94 ± 2.02	8.46±0.00

** Indicates the percentage of volume exposed to a dose equal or higher than the average value in each tissue section (i.e. previous column).*

SUPPLEMENTAL TABLE 1. Average physical parameters summary for each dissected tissue section. The error is reported as +/- 1 SD.

days 0-2

a	A1	A2	A3	A4	Sphere
1	3.37	4.09	3.38	3.46	3.39
-1	3.13	3.53	3.06	3.05	0.05
-2	2.96	3.15	2.86	2.73	1.14E-04
-3	2.75	2.73	2.62	2.21	8.82E-06
-4	2.48	2.27	2.33	1.37	2.21E-06
-5	2.16	1.83	2.00	0.77	9.40E-07
-6	1.83	1.43	1.68	0.49	5.28E-07
-7	1.51	1.09	1.38	0.34	3.49E-07
-8	1.25	0.85	1.14	0.26	2.56E-07
-9	1.05	0.69	0.96	0.20	2.00E-07
-10	0.89	0.58	0.82	0.17	1.65E-07

days 2-5

a	B1	B2	B3	B4	Sphere
1	1.74	2.08	1.69	1.72	1.70
-1	1.51	1.63	1.57	1.52	0.02
-2	1.36	1.34	1.50	1.39	5.73E-05
-3	1.20	1.05	1.40	1.23	4.41E-06
-4	1.02	0.78	1.28	1.03	1.11E-06
-5	0.84	0.56	1.15	0.81	4.70E-07
-6	0.68	0.40	1.01	0.62	2.64E-07
-7	0.55	0.29	0.88	0.47	1.75E-07
-8	0.45	0.23	0.77	0.37	1.28E-07
-9	0.38	0.18	0.67	0.30	1.00E-07
-10	0.33	0.15	0.60	0.25	8.27E-08

days 5-11

a	C1	C2	C3	C4	Sphere
1	1.57	2.16	1.58	1.92	1.55
-1	1.37	1.98	1.41	1.69	0.02
-2	1.25	1.87	1.30	1.08	5.24E-05
-3	1.11	1.72	1.16	0.15	4.04E-06
-4	0.96	1.50	1.02	0.04	1.01E-06
-5	0.80	1.14	0.88	0.02	4.30E-07
-6	0.67	0.79	0.73	0.01	2.42E-07
-7	0.55	0.56	0.60	0.01	1.60E-07
-8	0.46	0.42	0.47	0.01	1.17E-07
-9	0.40	0.34	0.38	0.00	9.18E-08
-10	0.34	0.28	0.32	0.00	7.56E-08

days 11-14

a	D1	D2	D3	D4	Sphere
1	1.78	2.65	2.77	1.71	1.73

-1	1.61	2.26	2.37	1.60	0.02
-2	1.49	1.95	2.16	1.52	5.85E-05
-3	1.35	0.98	1.94	1.42	4.51E-06
-4	1.13	0.36	1.71	1.30	1.13E-06
-5	0.77	0.18	1.47	1.15	4.80E-07
-6	0.48	0.11	1.22	0.99	2.70E-07
-7	0.32	0.08	1.00	0.84	1.78E-07
-8	0.24	0.06	0.83	0.72	1.31E-07
-9	0.18	0.05	0.70	0.61	1.02E-07
-10	0.15	0.04	0.60	0.53	8.44E-08

SUPPLEMENTAL TABLE 2. Generalized equivalent uniform dose (gEUD) for the dose distributions reported in Supplemental Figure 5.